Chapter 4
Metallization in Solar Cell

Formation of ohmic metal contacts to diffused and non-diffused Si wafers is perhaps the single most critical process in solar cell fabrication; it is also the final step. Figure 4.1 illustrates a broad range of solar cell metallization schemes classified in terms of processing temperature; three major categories are identified below.

Low Temperature
Lowest process temperature (< 200 °C) is based on the elegant HIT solar cell concept described in Chap. 1. The metal contact is formed with conductive and transparent thin ITO films on doped a-Si/c-Si interfaces. Thicker metallization for extracting current is provided with low temperature electroplating or polymer-based conductive pastes. ITO contacts on p-type c-Si have also exhibited promising results [1]. While ITO approach to metallization is attractive, it requires vacuum equipment and is considerably more expensive than the screen-printed contact.

Low and High Temperatures
This is a hybrid approach in which one of the contacts, usually the rear surface, is formed at high temperature, while the second contact is based on thin metal-silicide interface film formed at ~ 400 °C from among a broad range of metals including Ni, W, Mo, Pt, Pd, Ti, and Ag; subsequent thicker metallization is usually based on Cu or Ag electroplating [2]. In most cases, the metal-silicide process requires vacuum processing with some exception such as electroless Ni deposition [3].

High Temperature
This metallization scheme is based on high temperature annealing of screen-printed metal contacts and is the least expensive and most widely used method in the industry [4]. High temperature screen-printed metallization is the primary focus of this chapter.

In order to describe metal/Si interfaces, it is useful to review wafer resistance and metal contact resistivity measurements including relevant analytical formalisms. Accordingly, the rest of this chapter has been divided into the following subsections:

© Springer Nature Switzerland AG 2021

S. H. Zaidi, *Crystalline Silicon Solar Cells*,
https://doi.org/10.1007/978-3-030-73379-7_4

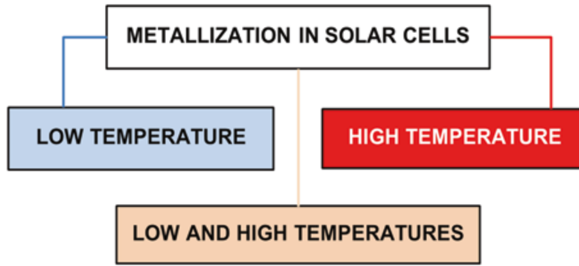

Fig. 4.1 Classification of metallization in solar cells in terms of process temperature

(i) Resistance Measurements in Si Wafers
(ii) Metal/Si Contact Resistivity Measurements
(iii) Geometric and Thermal Annealing Measurement Configurations
(iv) Screen-Printed Al/Si Metallization
(v) Screen-Printed Ag/Si Metallization

All the five topics are described in extensive detail below.

4.1 Resistance Measurements in Si Wafers

The resistivity, ρ (ohm-cm), and dopant concentration, N (atoms/cm^3), in Si a wafer are related by [5]

$$\rho = \left(Ne\mu\right)^{-1}, \tag{4.1}$$

where e is the electronic charge (A-sec) and μ the majority carrier mobility (cm^2/(V sec)). In Si solar cells, N is generally ~ 5E15/cm^3, μ is ~ 1000, and e = 1.6E-19 giving ρ of ~1.25 ohm-cm. Therefore, measurement of wafer resistivity determines its dopant concentration.

The resistance of any material with geometry of a rectangular block (Fig. 4.2a) is defined by

$$R = \rho \frac{L}{A}, \tag{4.2}$$

where ρ is the resistivity of the material. With L as the length, and A the cross-sectional area (WxH), Eq. 4.2 is rewritten as

$$R = \rho \frac{L}{WH} = R_{SH} \, {}^{L}\!/_{W}, \tag{4.3}$$

with R_{SH} defined by

$$R_{SH} = {}^{\rho}\!/_{H}. \tag{4.4}$$

For thin conducting layer on a wafer with thickness H = T (Fig. 4.2b), the resistivity is then simply given by

$$\rho = R_{SH} T. \tag{4.5}$$

In Eq. 4.5, the sheet resistance is often defined in terms of Ω/square (□) since from Eq. 4.3, $R = R_{SH}$ for L = W, i.e., for a square block.

A simple two-point measurement is ineffective when the resistance of the probe/sample interface is comparable to the sample itself; therefore, separate probes are used to measure voltage and current in order to accurately determine resistance. Figure 4.3a illustrates a typical four-point probe system for sheet resistance measurements [6]. The four probes are equally spaced tungsten metal tips supported by springs at the other end to minimize damage during measurement with typical spacings of ~ 1 mm. Figure 4.3b describes schematic for measurements in which two voltage probes (2 and 3) are used to measure voltage across the semiconductor as current is passed through it through external probes (1 and 4). This method is used to measure resistivity of bulk and thin samples based on simple mathematical formulism described below.

In case of bulk samples with thickness and areal dimensions far larger than the probe spacing, current flow is across a semispherical surface. The differential resistance dR=ρdx/A, integrated over this surface between two inner probes, is given by

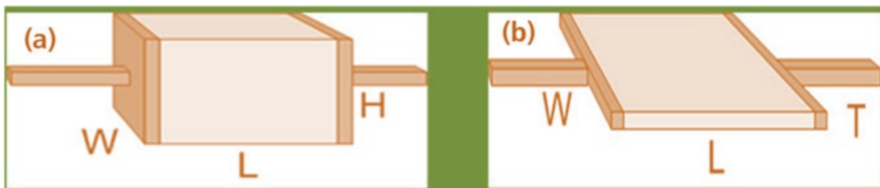

Fig. 4.2 Resistance calculations for (**a**) square block (**a**) and thin sheet (**b**)

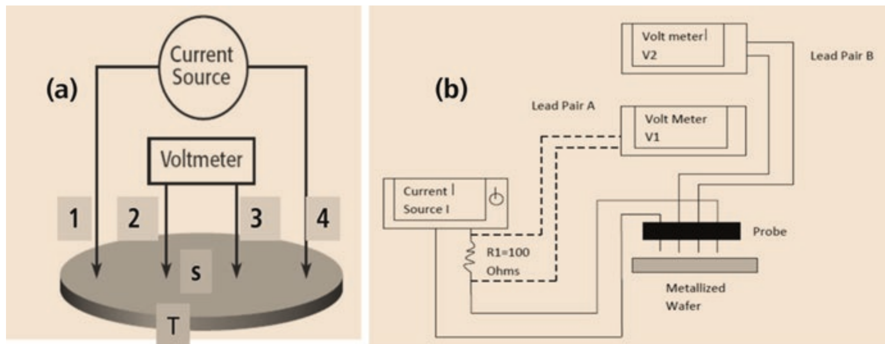

Fig. 4.3 Concept of the four-point probe system (**a**) and its circuit schematic for R_{SH} measurements (**b**)

$$R = \int_{x1}^{x2} \rho\, dx / 2\pi x^2 = \rho / 2\pi \left[-\frac{1}{x} \right] = \rho / 2\pi \left(\frac{1}{2s} \right). \tag{4.6}$$

For the probes, the resistance R is V/(2I) due to superposition of current at two tips; thus, the resistivity for a bulk ample is given by

$$\rho = 2\pi s \frac{V}{I}, \tag{4.7}$$

is a function of spacing between probe tips.

For the case of thin sheet with probe spacing far larger than the material thickness (t), current flow is in a circular ring with cross-sectional surface area A = 2πx*T, and differential resistance is then given by

$$R = \int_{x1}^{x2} \rho\, dx / 2\pi x T = \frac{\rho}{2\pi t} \ln(x)_s^{2s} = \frac{\rho}{2\pi T} \ln(2). \tag{4.8}$$

From the relationship between R_{SH} and thickness in Eq. 4.5, Eq. 4.8 can be rewritten as

$$R_{SH} = k \frac{V}{I} = 4.5324 \frac{V}{I}. \tag{4.9}$$

Equation 4.10 represents the general expression for four-point probe measurements with the geometrical $k = \pi / \ln(2) = 4.5324$.

Measurement system described in Fig. 4.3 has been used to determine sheet resistance of processed Si wafers; typical R_{SH} values have been summarized in Table 4.1. For lightly doped, n- and p-type wafers, current and voltages are low due to high resistance. By multiplying R_{SH} values with wafer thickness of T = 0.02 cm (Eq. 4.5), respective measured resistivity values of ~ 5.4 and 2.4 Ω-cm are in good agreement with wafer specifications provided by the manufacturer. Following n- and p-type diffusions, both current and voltage increases follow Ohm's law reflecting substantial reduction in resistance of doped thin layers; the system is able to measure ITO film sheet resistance.

Table 4.1 Representative R_{SH} measurements

Configuration	Voltage (mV)	Current (mA)	R_{SH}Ω/square
n-Si wafer	14.0	0.234	271.0
p-Si wafer	18.0	0.69	118.2
n/p Si wafer	74.7	5.83	58.0
n^+/p Si wafer	48.5	6.24	35.2
n^{++}/p Si wafer	26.0	7.85	15.0
p^{++}/p Si	31.0	6.85	20.5
ITO film on Si	27.0	6.53	18.7

4.2 Resistivity Measurements of Metal/Si Interface

Metal/Si interface resistivity is inherently difficult to measure accurately due to its sensitive dependence on geometrical and physical parameters. Figure 4.4 describes three ubiquitous metal/Si interfaces in solar cell and integrated circuit applications. In Fig. 4.4a, high temperature interaction between metal and Si results in the formation of metal/Si alloyed region underneath the metal. A good example of this type of contact is Al/Si interface. Figure 4.4b represents a case in which the metal reacts with diffused Si region. Metal/Si interaction can be at lower temperature to form silicide followed by thickening with electroplating, or it can be tailored into a single high temperature process to form an ohmic contact such as the Ag/n^+-Si screen-printed contact. The configuration in Fig. 4.4c represents an abrupt interface between metal and Si surface. A good example of this configuration is the interface between conductive thin films and Si wafers.

The contact resistivity formalism described here is based on extensive literature on semiconductor physics and devices; the author has relied mostly on references [6–12]. The current flow across metal/Si interface is a function of the depletion region inside Si; which it is dominated by two parameters:

(i) Thermionic emission (TE) in which electrons jump across the wide depletion region that is reduced because of the metal-induced image force.
(ii) Field emission (FE) in which electrons tunnel through a narrow depletion region formed by high doping at the semiconductor surface; FE is the preferred conduction mode in semiconductors.

Relative strength of these two carrier transport mechanisms is a function of several parameters including metal, temperature, doping density, dielectric constant, and electronic charge. The tunneling probability is defined by

$$E_0 = \frac{qh}{2}\left[\frac{N}{m^*\epsilon}\right]^{\frac{1}{2}}, \tag{4.10}$$

where q is the electronic charge, h the Planck's constant, N the doping concentration, and m^* the effective mass of tunneling carriers. In case of metal/Si Schottky barrier,

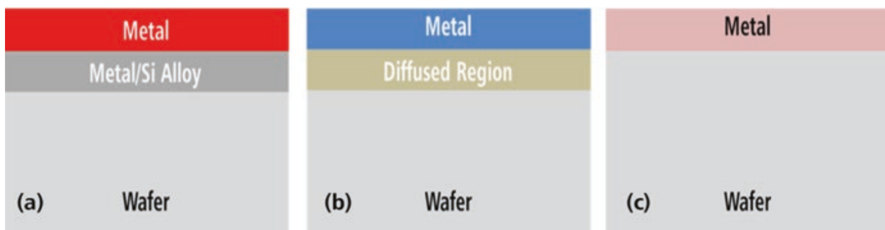

Fig. 4.4 Typical metal/Si interfaces in solar cells, microelectronics, and optoelectronics

$$\frac{KT}{E_0} \gg 1, \tag{4.11}$$

with carrier transport based primarily on thermionic emission and KT representing the mean free path length of the carrier; K is the Boltzmann constant. For ohmic contacts, the carrier transport is primarily based on field emission with

$$\frac{KT}{E_0} \gg 1, \tag{4.12}$$

either at very low temperatures or high doping densities. Based on semiconductor carrier transport equations, the contact resistivity is defined approximately as

$$\rho \sim \exp\left[\frac{q\varnothing_B'}{E_0 \coth\left(\frac{E_0}{KT}\right)}\right], \tag{4.13}$$

for both TE and FE cases and $\varnothing_B'$ is an effective barrier potential at the metal/semiconductor interface and illustrated in Fig. 4.5 for all three cases.

By extrapolating behavior of the coth function in Eq. 4.13, functional form for contact resistivity for both TE and FE cases can be determined:

$$\coth\left(\frac{E_0}{KT}\right) = \frac{e^{\frac{E_0}{KT}} + e^{-\frac{E_0}{KT}}}{e^{\frac{E_0}{KT}} - e^{-\frac{E_0}{KT}}}. \tag{4.14}$$

In the TE case, $\frac{E_0}{KT} \ll 1$, therefore, using Taylor expansion for exponential functions in Eq. 4.14, coth function is reduced to

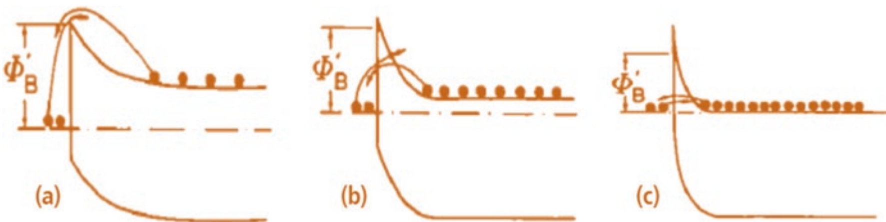

Fig. 4.5 Semiconductor carrier transport mechanisms for metal/n-semiconductor interface for three cases: (**a**) thermionic emission, (**b**) thermionic and field emission, and (**c**) field emission. Note that the barrier height has been reduced from its original value of $\varnothing_B$ to $\varnothing_B'$ due to image force lowering

$$\frac{1}{\coth\left(\frac{E_0}{KT}\right)} = \frac{E_0}{KT}. \quad (4.15)$$

Therefore, for the TE case, contact resistivity is approximated by

$$\rho_{TE} \sim \exp\left[\frac{q\phi'_B}{KT}\right]. \quad (4.16)$$

In the FE case, $\frac{E_0}{KT} \gg 1$, Eq. 4.14 is simply reduced to 1; therefore, the resistivity is given by

$$\rho_{FE} \sim \exp\left[\frac{q\phi'_B}{E_0}\right]. \quad (4.17)$$

Therefore, neglecting temperature and tunneling effective mass, the contact resistivity is reduced by increasing doping concentration for FE case (Eq. 4.17) and reducing barrier height for TE case (Eq. 4.16).

4.2.1 Resistivity Measurements in Vertical Configuration

Figure 4.6a illustrates vertical contact configuration for equipotential metal/semiconductor interfaces for uniform current flow between points A and B. In this configuration, the total resistance, R_T is given by

$$R_T = R_{AC} + R_{BC} + R_{Si} + R_{AM} + R_{BM}, \quad (4.18)$$

where R_{AC}, R_{AM} and R_{BC}, R_{BM} are contact and metal resistances at interfaces A and B, respectively, and R_{Si} is the semiconductor (Si) resistance. In most practical cases, $R_{AM} = R_{BM} = R_M \ll R_{AC}$, R_{BC} and R_{Si}; therefore, in case of identical metals at both interfaces, Eq. 4.18 can be rewritten as

$$R_T = 2R_C + R_{Si}. \quad (4.19)$$

With the expression for R_{Si} given by Eq. 4.3, for R_C is rewritten as

$$R_C = \frac{1}{2}\left(R_T - R_{SH}\frac{L}{W}\right). \quad (4.20)$$

For the vertical contact resistor configuration in Fig. 4.6a, the contact resistivity is simply R_C*A. Figure 4.7 plots current-voltage (I-V) response of identical 1 × 1 cm^2-area Al/Si contacts on 200-μm-thick, 1-ohm-cm, p-doped Si wafer. The total resistance of ~ 0.5 Ω from the slope of the I-V response is in good agreement for this type of contact. From Eq. 4.19, the contact resistivity is given by

$$\rho_C = R_C A = \frac{1}{2}\left(R_T A - \rho L\right) = 0.25 - 1.0\exp\left(-2\right) \sim 250\, m\Omega cm^2. \qquad (4.21)$$

which is in good agreement with low-resistance ohmic Al contacts to p-doped Si wafers. However, Eq. 4.21 is ill-suited for accurate low-resistivity measurements especially considering almost negligible contribution of the second term in the equation; therefore, Eq. 4.20 is used to drive an expression for R_T given by

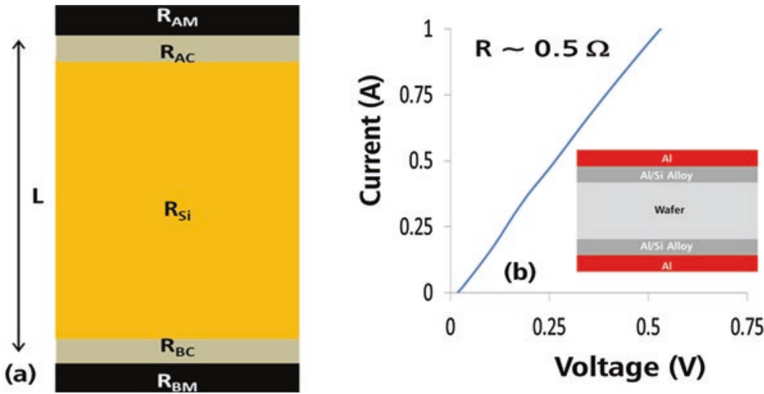

Fig. 4.6 Vertical contact configurations with identical surface areas (**a**) and plot of resistance versus distance of Al/Si contacts on p-doped Si wafer (**b**)

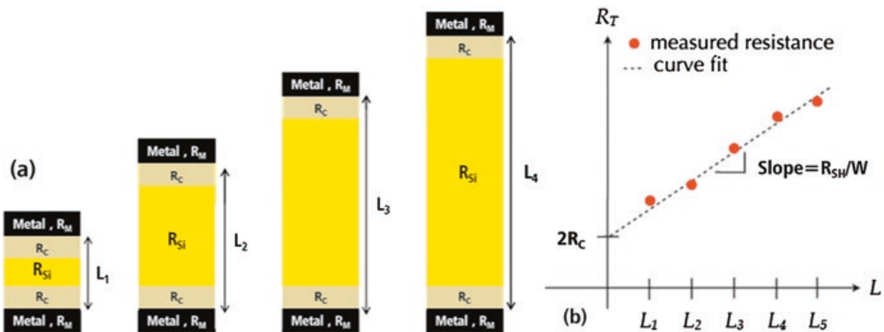

Fig. 4.7 Identical resistors of increasing length (**a**) and plot of their resistances as a function of their lengths (**b**)

$$R_T = 2R_C + R_{SH}\frac{L}{W}. \tag{4.22}$$

If several resistors of varying lengths with identical areas are fabricated (Fig. 4.7a) and their respective R_T measurements plotted as a function of distance (Fig. 4.7b), a linear response will be realized. In the limit of L = 0, $R_T = 2R_C$; the slope of the graph will be R_{SH}/W. In practice, vertical contacts are not compatible with wafer processing. Lateral or horizontal contacts are used for metal/semiconductor contact resistivity characterization.

4.2.2 Resistivity Measurements in Lateral Configuration

A lateral metal/semiconductor contact (Fig. 4.8a), similar to a vertical contact, is divided into three regions: metal, metal/semiconductor interface, and an un-doped or doped semiconductor region underneath. Current flow in the semiconductor and metal regions is along the horizontal direction. Away from the edges, current flow is approximately vertical at the metal/semiconductor interface, but close to the edges, there is a significant nonuniformity. Therefore, the physical area of the contact is not used for resistivity calculation. At the edges, especially for diffused contacts, current crowing effects are dominant (Fig. 4.8b). Detailed analysis reveals that the current flow across the contact interface close to the edge is approximated by

$$I(x) = I_0 \exp\left(\frac{x}{L_T}\right), \tag{4.23}$$

where L_T is defined as the transfer length at which from the edge of the contact, current flowing into the semiconductor layer is reduced by 1/e, i.e., 63% of the total current entering the metal layer. Sometimes, it is also referred to as the effective

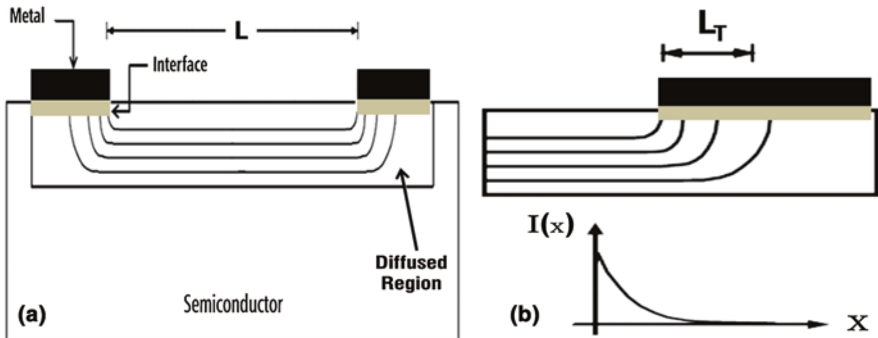

Fig. 4.8 Metal/semiconductor contacts in lateral configuration

contact width. Further away from the edge, there is no current flow across the metal/semiconductor contact. The transfer length is related to the contact resistivity and sheet resistance by

$$L_T = \sqrt{\frac{\rho_C}{R_{SH}}}. \tag{4.24}$$

Essentially, transfer length is the average distance an electron (or hole) travels before it flows into the metallic region. At low L_T values, current crowding is enhanced. Low L_T values are achieved by decreasing ρ_C or increasing R_{SH}. In contrast, for large L_T values, the lateral contact current flow behavior approaches the vertical limit. High L_T values are achieved by increasing ρ_C or decreasing R_{SH} Semiconductor carrier transport analysis reveals contact resistance for such interfaces can be modeled by

$$R_C = \frac{L_T}{W} R_{SH} \coth\left(d/L_T \right), \tag{4.25}$$

where d is the contact width and W its length. Based on the behavior of $\coth\left(d/L_T \right)$ function, two limits of R_C are realized:

$$\frac{d}{L_T} \gg 1, \coth\left(d/L_T \right) \sim 1, \tag{4.26}$$

$$\frac{d}{L_T} \ll, \coth\left(d/L_T \right) \sim \frac{L_T}{d}. \tag{4.27}$$

By inserting Eqs. 4.26 and 4.27 in Eq. 4.25, an expression for ρ_C for the diffused metal/semiconductor interface is given by

$$\rho_c = R_C W L_T. \tag{4.28}$$

Hence, for diffused contacts, contact resistivity is independent of its width and virtual physical contact area is WL_T. Using Eqs. 4.24 and 4.27 in Eq. 4.25, an expression for ρ_C approximating vertical configuration is given by

$$\rho_c = R_C W d. \tag{4.29}$$

Therefore, the contact resistivity is simply contact resistivity multiplied by the actual physical area (Eq. 4.21), the same as its vertical configuration.

Transmission line method (TLM) is extensively used on account of its simplicity, reliability, and accuracy. The TLM method, originally proposed by Shockley, provides a convenient method to determine ρc for lateral metal/semiconductor

contacts. In contacts with identical geometry and physical properties separated by increasing distances (Fig. 4.9), an expression for total resistance, R_T, can be derived by combining Eqs. 4.22 and 4.28 and is given by

$$R_T = \frac{R_{SH}}{W}\left(2L_T + L\right). \tag{4.30}$$

From Eq. 4.30, it is noted that for $L = 2L_T$, $R_T = 0$ and at $L = 0, R_C = \frac{R_T}{2}$. Plotting R_T as a function of L for a series of identical resistors, R_C and R_{SH} can be determined (Fig. 4.10). This methodology is extensively applied in characterization of screen-printed Al and Ag contacts on un-doped p-type and doped n/p Si wafers in later sections of this chapter.

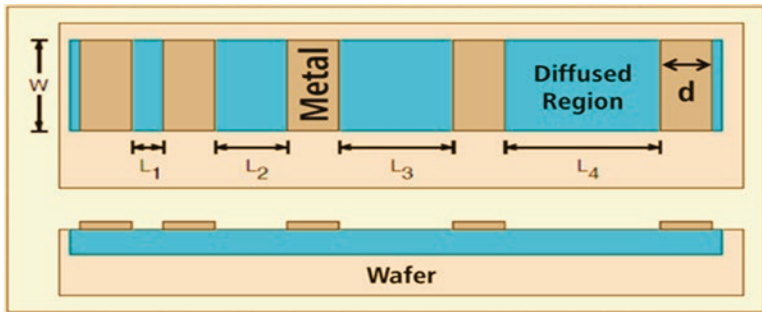

Fig. 4.9 Metal/semiconductor contacts arranged in TLM configuration for resistivity measurements

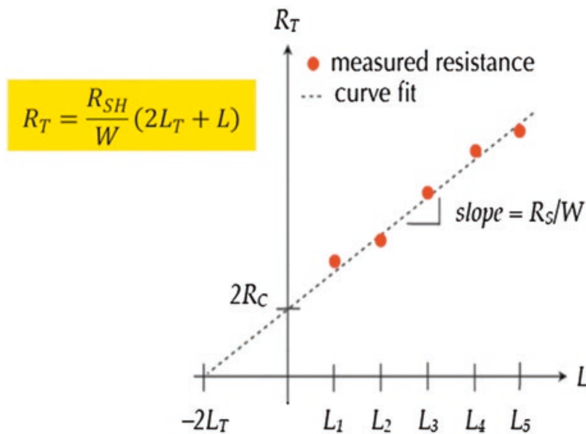

Fig. 4.10 R_T plotted as a function of distance in TLM configuration

4.3 Geometric Configurations

Contact resistivity is a function of many parameters including area (both physical and virtual), distance, doping, temperature, and metal type. Screen printing-based geometric patterns were designed to understand and evaluate metal/Si contact interface. By varying the area, contact resistivity variations can be evaluated for both diffused and non-diffused surfaces since the contact resistivity is expected to vary significantly for both cases. Similarly, distance variation while keeping the same area will help establish layer uniformity. Figure 4.11 shows pictures of the screen print masks investigated in this study. The minimum surface area was $.25 \times .25$ mm^2 and the largest was 10×20 mm^2. Succinct features of these masks have been summarized in Tables 4.2 and 4.3. Relatively large dimensions were chosen to correlate with solar cell contact designs; the pattern in Fig. 4.11a has been used extensively for contact characterization. For the largest metal pad dimensions of 10×20 mm^2, step sizes were 2.5, 5, 10, and 20 mm (last row in Table 4.2).

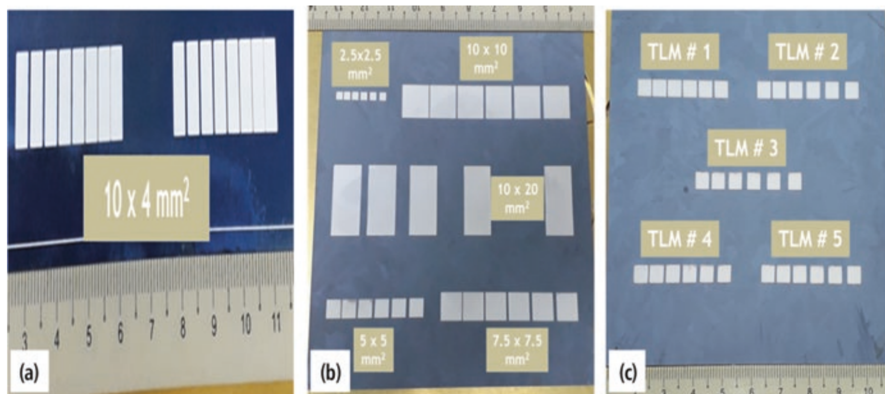

Fig. 4.11 Screen-printed metal pads on Si wafers showing varying areas and separations: (**a**) 10×4 mm^2, (**b**) 2.5×2.5 mm^2 to 10×20 mm^2, and 2.5×2.5 mm^2 patterns with step size varying from 0.1 mm to 0.5 mm

Table 4.2 Contact pad dimensions and separations

Pad dimensions (mm^2)	Minimum separation (mm)	Step size (mm)
0.25×0.25	0.3	0.2
0.5×0.5	0.3	0.2
0.75×0.75	0.3	0.2
10×10	0.3	0.2
4×10	0.1	0.1
10×20	2.5	5,10,20

Table 4.3 Contact pad step size variations

Mask # (mm^2)	Minimum separation (mm)	Step size (mm)
1	0.3	0.1
4	0.4	0.2
5	0.5	0.3
2	0.6	0.4
3	0.7	0.5

4.4 Thermal Annealing Configurations

Al and Ag screen-printed contacts in Si solar cells were simultaneously annealed in four thermal configurations. Summary of annealing configurations is given by:

(i) Wafer translation in horizontal orientation.
(ii) Wafer translation in vertical orientation.
(iii) Stationary wafer in horizontal orientation.
(iv) Stationary wafer in vertical orientation.

4.4.1 Conveyor Belt IR RTA Furnace

Figure 4.12a shows pictures of industrial-type conveyor belt IR furnace, manufactured by Radiant Technology Corporation, including its typical thermal profile with varying temperatures across its six zones (Fig. 4.12b). This furnace was used for much of the work reported here. The zone temperature and conveyor belt speed are adjusted in order to create any desirable thermal profile. In normal operation, conveyor belt transports screen-printed wafers across six temperature zones from one end to the other at constant speed of 75 inches per minute. The length of the heating zone was approximately 8 feet resulting in wafer transit time of 90 s. Figure 4.12b plots temperature as a function of time for high and low temperature profiles with the inset illustrating a conceptual drawing of the temperature versus time profile. Wafer travel time through the highest temperature zones is ~ 10 s. Horizontally oriented wafer encounters rapid temperature variations as it enters and exits heating zones. Heating is provided by high-power IR lamps. This kind of thermal annealing system is generally classified as an in-line rapid thermal annealing (RTA) IR conveyor belt furnace. It is an furnace industrial with power consumption of 45 kW.

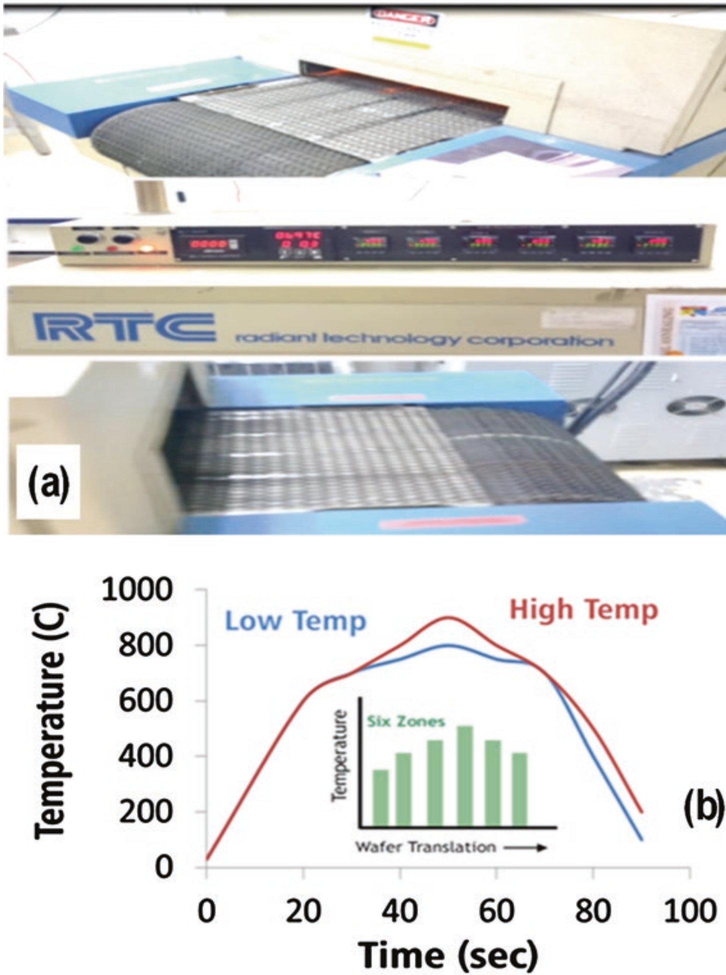

Fig. 4.12 Six-zone conveyor belt furnace (left) and its thermal profile (right) used for simultaneous annealing of Ag and Al screen-printed contacts on Si

4.4.2 Parallel-Plate Furnace

An inexpensive and low-energy alternative to IR RTA furnace was developed by replacing IR lamps with quartz halogen lamps in a parallel-plate configuration schematically described in Fig. 4.13a. A total of 12 (six at the top and six at the bottom) 500 W lamps were used in conjunction with 2 thermocouples at top and bottom lamp assemblies to controllably vary temperature as a function of time. Figure 4.14b

plots a typical temperature profile for this system. This furnace attains highest temperatures in about 60–90 s followed by rapid cooling down as lamps are turned off. In comparison with RTA, the wafer in parallel-plate furnace experiences high temperature for slightly longer duration; the ramp down is comparable. The wafer remains stationary as quartz lamps are tuned on; increase in wafer temperature is also assisted by light absorption since halogen light spectrum within Si bandgap. Power consumption of this furnace was 6 kW.

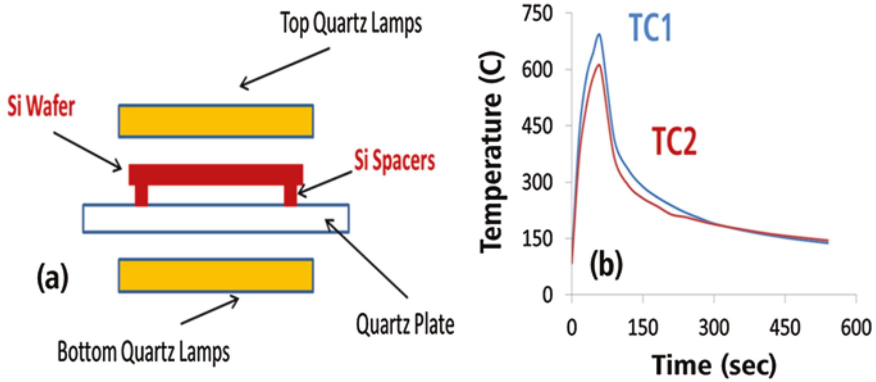

Fig. 4.13 Conceptual drawing of rapid thermal annealing system (**a**) and plot of approximate temperature variation as quartz lamps are turned on and off (**b**); the system is capable of annealing up to 6” x 6” wafers

Fig. 4.14 Conceptual drawing of quasi-rapid quartz furnace annealing system for up to 4” x 4” wafers

4.4.3 Quartz Tube Furnace

The third annealing configuration uses Lindberg/Blue M 1100 °C digital tube furnace with three independently controlled heating zones (STF55666C-1). A silicon carbide paddle, connected to a DC motor, moves the wafer in vertical orientation speed at a constant speed of 55 inches per minute across the 91-cm-long heating zones (Fig. 4.14). In this system, wafers enter and exit from the same input end; therefore, virtually symmetric six-zone temperature profile is achieved. This system, suitable for batch processing, represents highly uniform temperature distribution and is widely used in semiconductor processing for oxidation and diffusion applications. The temperature variation of this furnace is considerably slower in comparison with RTA and parallel-plate furnaces. Thermal annealing profile is depicted in Fig. 4.15 for typically low and high temperatures; inset illustrates the concept of virtual six-zone furnace. Heating is provided by resistive coils; there is minimal light absorption in the wafer. The wafer stays at high temperatures for about ~ 30–40 s. Quartz tube furnace power consumption is 11 kW.

4.4.4 Radial Furnace

An alternative to traditional quartz tube furnace was developed using quartz halogen lamps in a radially symmetric configuration illustrated in Fig. 4.16a. A total of 12 (six at one side and six on the other side) lamps each operating at 500 watt were used with respective thermocouples on either side used for controllable temperature variation. Figure 4.16 (b) describes a typical temperature profile for this system. The wafer remains stationary in vertical configuration. This furnace is capable of annealing up to 5”x5” wafers. Its volume is significantly larger than the quartz furnace with slowest heating and cooling down ramp rates; it takes ~ 7–8 min to reach desirable process temperatures. Thus, the wafer in this furnace stays at high temperatures

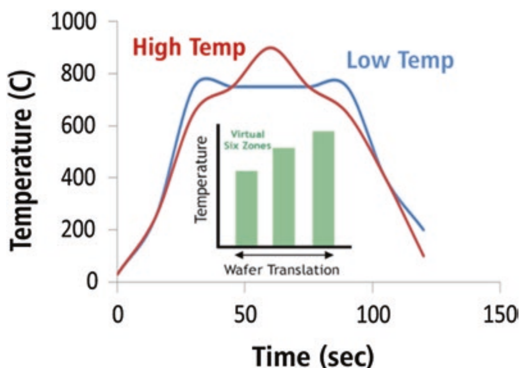

Fig. 4.15 Plot of approximate temperature variation as wafers travel in and out of the three-zone quartz furnace

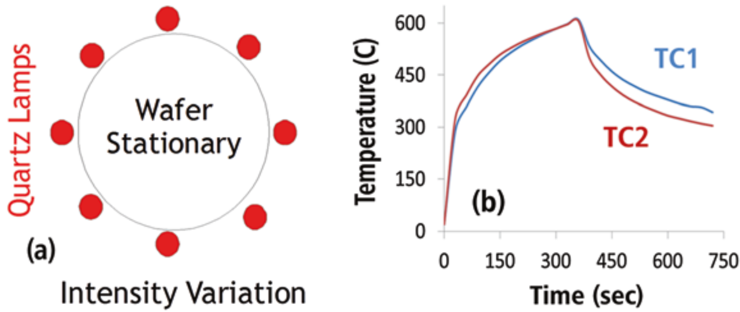

Fig. 4.16 Conceptual drawing of radially symmetric quasi-rapid thermal annealing system (**a**) and plot of typical temperature variation as quartz lamps are turned on and off (**b**); the system is capable of annealing up batch of 5” x 5” wafers

far longer than either of the three configurations described above. Radial furnace operates at 6 kW.

4.4.5 Summary of Annealing Configurations

Critical features of the four annealing furnaces are summarized below.

(i) Conveyor belt RTA furnace employs high-power IR lamps to heat the moving wafer in horizontal configuration at the highest ramp-up and ramp-down rates.
(ii) Parallel-plate furnace uses quartz halogen lamps with substantial light in the visible spectrum to heat a stationary wafer at ramp rates comparable to industrial RTA.
(iii) Quartz tube furnace heats slow-moving wafers in vertical configuration using IR heaters.
(iv) Radially symmetric furnace uses quartz halogen lamps to heat stationary wafers at the slowest ramp rates.

Relative energy consumption for the four furnaces is provided in Table 4.4. The energy calculations assume annealing times of 90 s for parallel-plate furnaces, 120 s for the quartz tube, and 450 s for radial furnaces. Lowest energy usage occurs in the parallel plate. However, in reality, quartz and radial furnaces represent the least energy consumption options because of their ability to process batch of wafers.

Table 4.4 Energy usage in RTA systems

RTA system	Energy usage (kwh)	Comment
Conveyor belt	1.1	In-line, single wafer
Parallel plate, RTA	0.15	In-line, single wafer
Quartz tube, quasi-RTA	0.75	Batch processing
Quartz tube furnace	0.37	Batch processing

4.5 Experimental Results

Metallization of Si wafers was carried with screen-printed pastes on single and multicrystalline, boron-doped wafers with bulk resistivity of 0.5–1.0 Ω.cm and thickness of 200 μm; relevant wafer processing steps have already been described in Chap. 2. Emitter sheet resistances of $POCl_3$ and H_3PO_4 diffusion process ranged from ~ 20 to 50 Ω/square. The screen-printed contacts were formed for Ag with Heraus SOL 9621M paste and for Al with Mono-Crystal Pase-1207. Screen-printed paste contacts were dried in an oven at 100 °C for 10 min followed by high temperature thermal annealing. A digital multimeter (ADM20) was used for resistance measurements between metal pads.

The following subsections present results on Ag and Al screen-printed contacts with respect to surface texture, contact area, and contact separation in order understand contact formation.

4.5.1 TLM Pattern Calibration

TLM versatility was investigated for a wide range of parameters. Conveyor belt RTA furnace was used for all the work presented in this subsection. Experimentally measured resistance data with respect to distance between adjacent metal pads was plotted and fitted with linear squares method. The expression for contact resistivity derived in Eq. 4.28 was used to determine Al/Si and Ag/Si contact resistivities.

4.5.2 Variation with Texture

Figures 4.17 and 4.18 plot measured resistance data from 0.4 × 1 cm^2 area TLM contacts on planar and textured surfaces; insets represent calculated R_C (Ω), L_T (in mm) and ρ_C (mΩ-cm^2) values. The linear squares fit of the experimental data revealed 99% accuracy levels. A comparison of R_C and ρ_C data shows lower values on textured surfaces by ~ 20% for Al and by ~ 30% for Ag, respectively. This reduction is likely to be a function of high temperature metal-silicon alloying; it will be discussed in sufficient detail as part of the morphological analysis of contact interfaces.

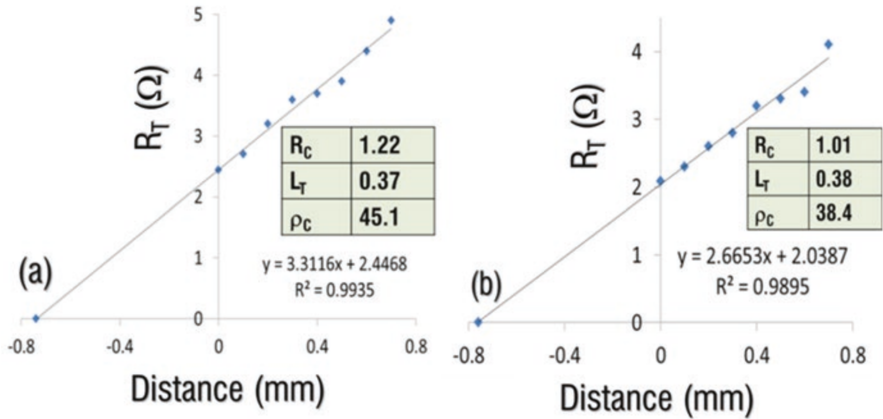

Fig. 4.17 Resistance measurements of identical Al TLM contacts on planar (a) and textured p-Si wafers; insets represent calculated R_C, L_T, and ρ_C values from the plotted data

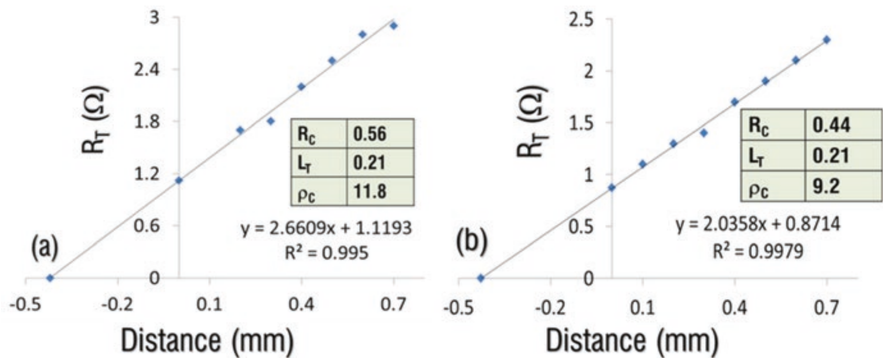

Fig. 4.18 Resistance measurements of identical Ag TLM contacts on planar (a) and textured n/p-Si wafers; insets represent calculated R_C, L_T, and ρ_C values from the plotted data

4.5.3 Variation with Area

Figure 4.19 plots R_C and ρ_C measurements as a function of Al/Si contact for areas in 0.0625–1-cm^2 range. A slowly varying reduction response is observed for R_C (Fig. 4.19a) and linear increase is observed for ρ_C (Fig. 4.19b). Both R_C and ρ_C responses were curve-fitted with ln (x) and linear (x) functions with reasonable accuracy; equations and statistical accuracy levels are also shown in Fig. 4.19. It is observed that R_C is approximately reduced by a factor of 2.5 and ρ_C increased by a factor of 2 as the area is increased from 0.0625 to 1 cm^2; L_T values were comparable for all measurements. For a resistor, resistance increases linearly with length and decreases inversely with area (Eq. 4.2). Since separation between the pads was identical for all areas, the only variable for measurements was contact area. The contact

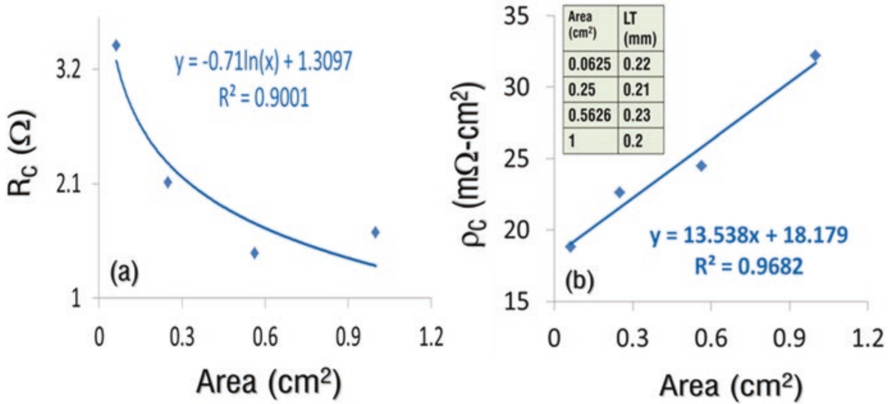

Fig. 4.19 Contact resistance (**a**) and resistivity measurements (**b**) of Al TLM contacts on p-Si wafer plotted as a function of pad area; inset in (**b**) represents L_T values utilized in ρ_C calculation

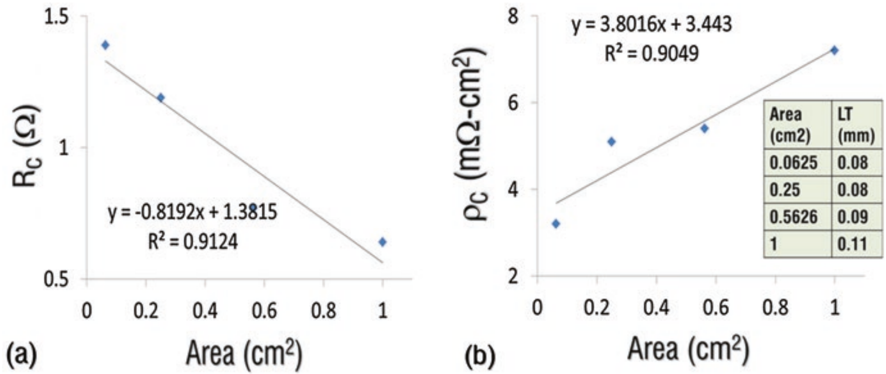

Fig. 4.20 Contact resistance (**a**) and resistivity measurements (**b**) of Ag TLM contacts on n/p-Si wafer plotted as a function of pad area; inset in (**b**) represents L_T values utilized in ρ_C calculation

area decreases by a factor of 16 from the largest to smallest pattern; however, R_C only increases by a factor of 2.5. Similarly, ρ_C is a linear function of transfer length, L_T, and contact length w (Eq. 4.28). Since L_T is the same for all patterns, the only variable is contact length, which decreases by a factor of 4 from the largest to smallest pattern; however, ρ_C only decreases by a factor of 2. In general, for ρ_C calculation, Eq. 4.28 holds true since R_C increases as contact length decreases. However, simple resistor analogy does not adequately describe Al/Si interface due to its dependence on ρ_C.

Figure 4.20 plots Ag/Si interface R_C and ρ_C measurements with respect to increase in contact area from 0.0625 to 1 cm^2. Similar to the Al contact, R_C exhibits linear reduction and ρ_C linear increase contact area increases. Both R_C and ρ_C responses were curve-fitted with linear (x) functions with reasonable accuracy; equations and statistical accuracy levels have been included in Fig. 4.20. It is

observed that that R_C is reduced by a factor of 2 and ρ_C increased by a factor of 2 for comparable L_T values. This behavior is similar to the Al contact. Therefore, R_C and ρ_C variations with contact area are comparable for Al/Si and Ag/Si contacts.

4.5.4 Variation with Distance

Figure 4.21 plots resistance response of identical area (0.25 cm^2) Al/Si contact as a function of separation in 0.1–0.5-mm range (Table 4.3). A reasonably good linear response is observed for both R_C and ρ_C; lack of better fit may be attributed to mismatch in L_T values and the variation in minimum distances for five TLM patterns. The measured data exhibits increase in resistance with distance as expected for a normal resistor. Figure 4.22 plots similar measurements for the Ag contact. For the Ag case, linear response for the R_C contact with area is pretty poor although ρ_C exhibits significantly superior linear response. The anomaly in R_C data may be attributed to considerable differences in L_T values that will significantly impact calculated R_C and ρ_C values. In general, both Al and Ag contacts exhibit good linear response as contact separation between pads increases typical of a normal resistor.

4.5.5 Variation with Largest Areas and Distances

Figure 4.23 plots R_T as a function of distance for the largest area (10 × 20 mm^2) pattern with the longest separation (20 mm). The insets in Fig. 4.23 show calculated R_C, ρ_C, and L_T values extracted from the R_T data. It is observed that calculated values

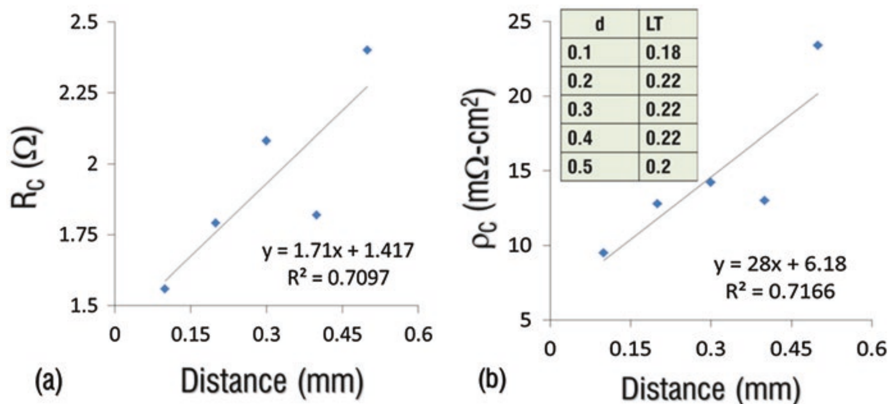

Fig. 4.21 Contact resistance (**a**) and resistivity measurements (**b**) of 0.25-cm^2-area Al TLM contacts on p-Si wafer plotted as a function of pad separation; inset in (**b**) represents L_T values utilized in ρ_C calculation

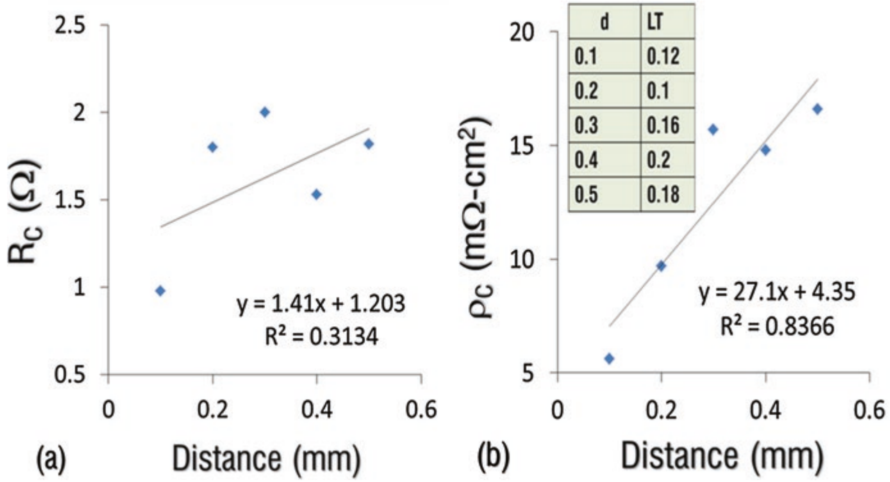

Fig. 4.22 Contact resistance (**a**) and resistivity measurements (**b**) of 0.25-cm^2-area Ag TLM contacts on n/p-Si wafer plotted as a function of pad separation; inset in (**b**) represents L_T values utilized in ρ_C calculation

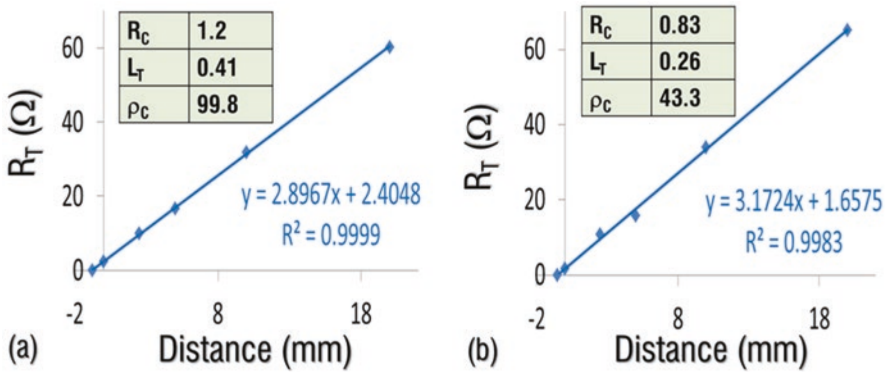

Fig. 4.23 Resistance variation of largest area TLM pattern plotted as a function of distance for (**a**) Al and (**b**) Ag; also shown in insets are the calculated L_T and ρ_C values

(R_C, ρ_C, and L_T) for both Al and Ag contacts are significantly higher. A summary of key features in presented in Table 4.5 by calculating ratios with respect to 10 × 20-mm^2 area patterns. It is observed that R_C is ratio increases by 2 and ρ_C reduced by 2.

This behavior is consistent with our earlier observations, i.e., R_C generally decreases as contact areas are reduced and ρc increases with length of the contact. This was also revealed by R_C and ρc calculations based on mathematical fits in Figs. 4.22 and 4.23. The calculated values for 20-mm separation lead to values far higher than observed in Fig. 4.23.

Table 4.5 Summary of Al and Ag ρc and R_C ratios

Area (mm^2)	Length	Area	Al ρ_c	Al R_c	Ag ρ_c	Ag R_c
2.5 × 2.5	8	32	5.3	0.35	13.5	0.6
5 × 5	8	8	4.4	0.57	8.5	0.7
7.5 × 7.5	8	3.5	4.1	0.84	8.0	1.1
10 × 10	8	2	3.1	0.74	6.0	1.3

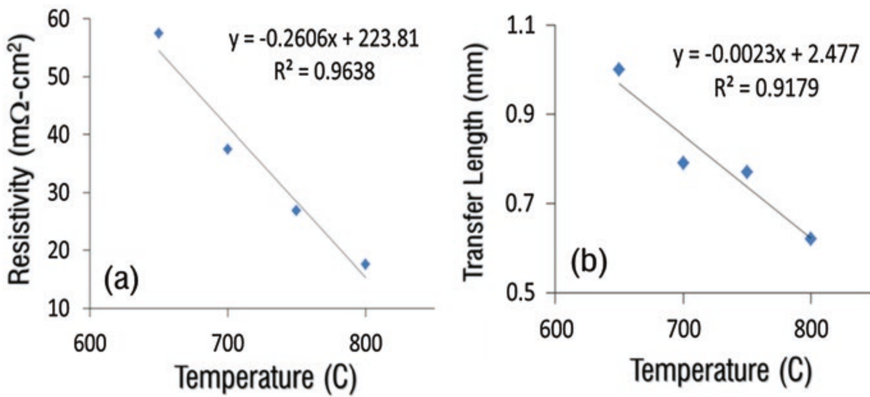

Fig. 4.24 Al contact resistivity (**a**) and transfer length (**b**) variation with temperature in radially symmetric quasi-rapid thermal annealing furnace

4.6 Aluminum Contact Variation with Annealing Configurations

The principal objective of annealing experiments is to determine least energy consumption approach to optimum Al/Si contact formation. This study will also help enhance our physical understanding of calculated parameters R_C, ρ_C, R_{SH}, and L_T. For all measurements in the following sections, R_T vs distance data is plotted and curve-fitted at each temperature profile in order to extract R_C, ρ_C, R_{SH}, and L_T parameters (Eq. 4.22, Figs. 4.7 and 4.10). These parameters are then plotted as a function of temperature.

4.6.1 Al/Si Contact in Radial Furnace

In radial furnace, wafers in vertical orientation are stationary with halogen quartz lamps serving as heating source. Resistance data as a function of distance is acquired with varying thermal profiles (Fig. 4.16b). Figure 4.24 plots calculated ρ_C and L_T values as a function of temperature. It is observed that as temperature increases, both these parameters decrease linearly with statistical accuracy of 96% to 92%. In order to compare with calculated R_{SH} values, Al films were etched off the contact regions at room temperature

in hydrochloric acid (HCl) solution. Figure 4.25 plots calculated and measured R_{SH} values as a function of temperature. Calculated R_{SH} values are curve-fitted with a third-order polynomial function, while measured R_{SH} values exhibit linear response with 99% statistical accuracy; no correlation is observed between calculated and measured values. Calculated R_{SH} values, even if curve-fitted well with third polynomial function, appear to remain invariant with temperature since such small variations lie well within experimental errors. In contrast, measured R_{SH} values exhibit linear reduction from ~ 70 to 30 Ω/square. Additional insight is gained by examining the four-point data given in Table 4.6. As annealing time and temperature increase, linear response in voltage and current is observed, i.e., reduction in voltage and increase in current. Hence, increasing current corresponds to increasingly conductive Si layer.

4.6.2 Al/Si Contact in Quartz Tube Furnace

In quartz furnace, vertically oriented wafers slowly transit across a virtual six-zone temperature profile (Figs. 4.14 and 4.15) with IR lamps serving as heating source. A more detailed study on Al/Si contact formation in this furnace has been reported

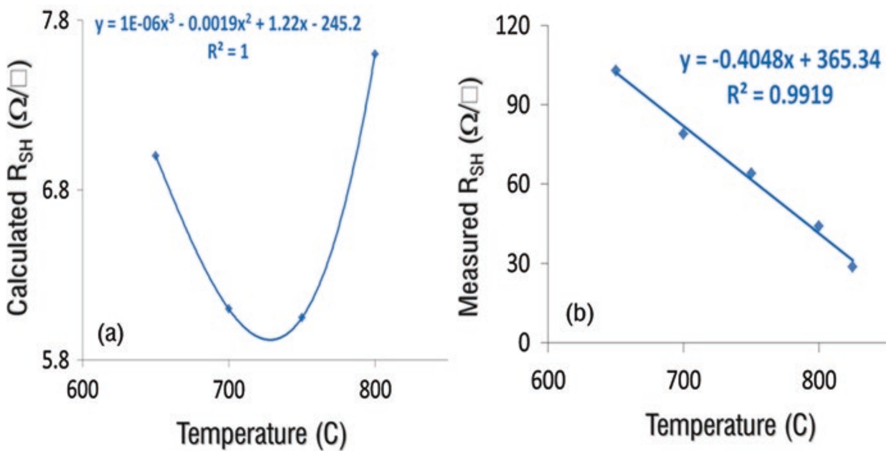

Fig. 4.25 Al calculated sheet resistance (**a**) and measured sheet resistance (**b**) in radially symmetric quasi-rapid thermal annealing furnace

Table 4.6 Al Sheet resistance measurements in radial furnace

Anneal time (sec)	Voltage (mV)	Current (mA)	R_{SH} Ω/square
180	58.8	3.71	71.8
210	53.0	4.88	49.2
360	44.0	6.14	32.5
720	26.0	7.14	16.5

elsewhere [12]; representative data is presented for high and low temperature profiles. Figure 4.26 plots R_T variation with distance for low (700/700/700) temperature annealing profile; inset provides calculated values of R_C, ρ_C, and L_T at hold times of 30 and 40 s. Values of R_C, ρ_C, and L_T decrease substantially with annealing time with resistivity lower than that observed in radial furnace. Figure 4.27 shows similar measurements at higher (600/600/900 and 600/600/925) temperature profiles.

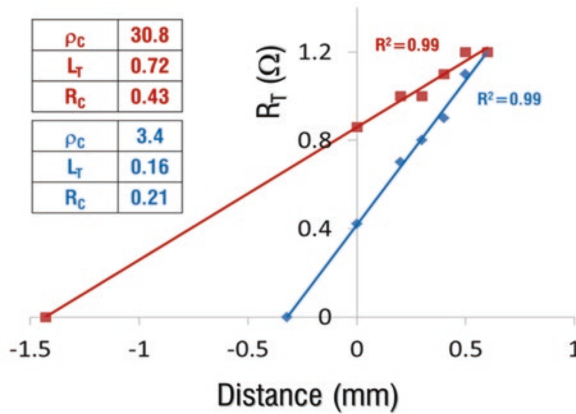

Fig. 4.26 Measured Al R_T as a function of distance for 700/700/700 temperature profile, red line for 30-sec and blue line for 40-sec anneal times; insets show calculated ρ_C, L_T, and R_C values

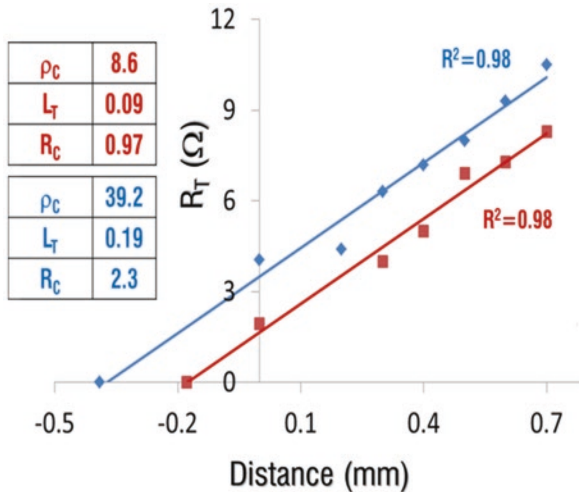

Fig. 4.27 Measured Al R_T as a function of distance for 600/600/900 and 600/600/925 temperature profiles, red line for 10-sec and blue line for 5-sec anneal times; insets show calculated ρ_C, L_T, and R_C values

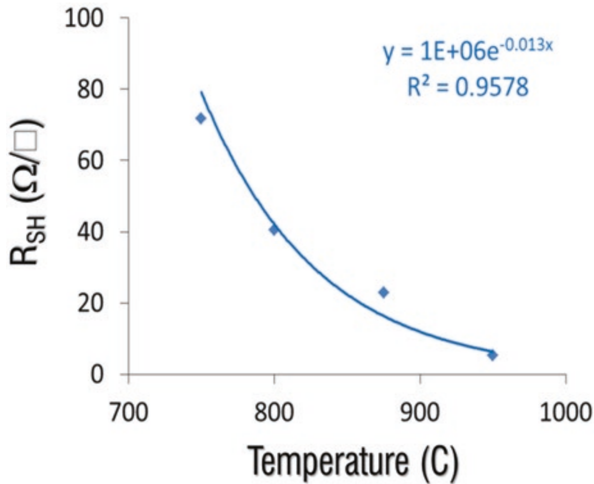

Fig. 4.28 Measured sheet resistance in conventional quartz tube furnace for temperature profiles described in Fig. 4.15 after removal of Al

Table 4.7 Al sheet resistance measurements in quartz tube furnace

Anneal profile	Voltage (mV)	Current (mA)	R_{SH} Ω/square
600-600-850 (10 s)	48	2.94	74
700/700/700 (45 s)	56	4.9	51.8
600-600-875 (10 s)	37	6.54	25.6
600-600-925 (0 s)	9.6	8.78	4.95

Similar to 700/700/700 profile, longer annealing time leads to lower resistivity. Comparison of low and high temperature profiles reveals that lower resistivity is achieved at lower temperature and longer time. Figure 4.28 plots measured R_{SH} as a function of temperature for temperature profiles in Figs. 4.26 and 4.27. It is observed that temperature-based reduction in R_{SH} exhibits slow exponential response with lowest ρc of ~ 5 Ω/square. The four-point data in Table 4.7 also supports this trend through substantially higher current flow consistent with lowest resistivity.

4.6.3 Al Contact in RTA Furnace

In RTA, wafers in horizontal orientation rapidly travel across six-zone temperature profile (Fig. 4.12) with IR lamps serving as heating source. A more detailed study on Al/Si contact in this furnace has been reported elsewhere [12]; additional

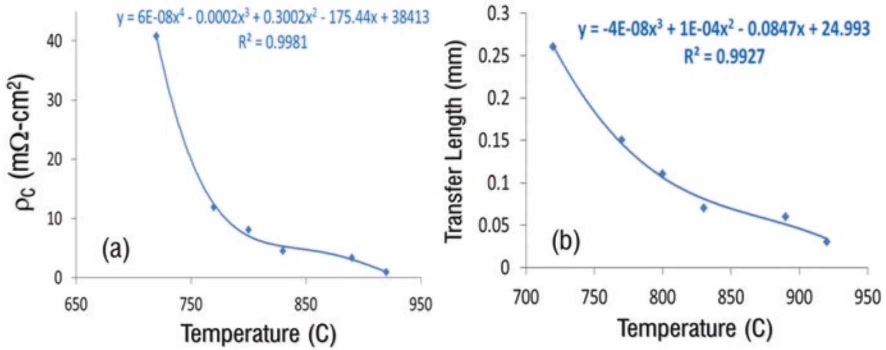

Fig. 4.29 Al contact resistivity (**a**) and transfer length (**b**) variation with temperature in conveyor belt rapid thermal annealing furnace

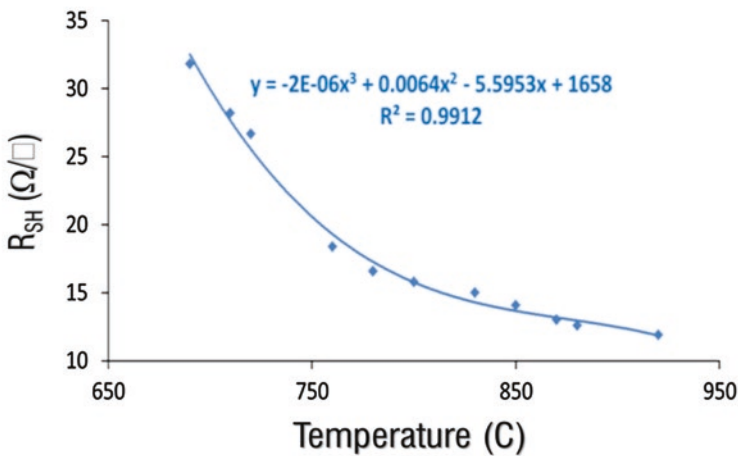

Fig. 4.30 Measured sheet resistance plotted as a function of temperature in conveyor belt RTA furnace after removal of Al

features are presented. Figure 4.29 plots ρ_C and L_T measurements as a function of temperature. Both ρ_C and L_T exhibit reduction with increasing temperature with respective responses curved-fitted with fourth- and third-order polynomials. Contact resistivity deceases rapidly at lower temperatures; at higher temperatures, the rate of reduction is relatively low. Reduction on sheet resistance with temperature is approximated to be with a third-order polynomial (Fig. 4.30). A comparison of four-point measurements of RTA furnace (Table 4.8) with quartz furnace (Table 4.7) reveals a similar behavior except for the higher current flow for the latter case.

Table 4.8 Al sheet resistance measurements in RTA furnace

Anneal Temperature (°C)	Voltage (mV)	Current (mA)	R_{SH} Ω/square
660	59	3.02	88.5
670	53	5	48
710	41	7.25	25.6
900	21	8.04	5

4.6.4 Al Contact in Parallel-Plate Furnace

In parallel-plate furnace, the wafer in the horizontal orientation is stationary with halogen quartz lamps serving as heating source. Resistance data is acquired as a function of distance with varying thermal profiles (Fig. 4.13b). Figure 4.31 plots calculated ρ_C and L_T values as a function of temperature. It is observed that as temperature increases, ρ_C decreases linearly, while L_T reduction response is approximately modeled with third-order polynomial. Figure 4.32 and Table 4.9 provide R_{SH} data for temperatures in ~ 650–900 °C range. Sheet resistance variation is curve-fitted with a slowly varying exponential function. The measured sheet resistance variation with temperature (Table 4.9) matches well with RTA and quartz furnaces except with higher R_{SH} values.

4.6.5 Summary of Al/Si Contact Formation

Four different types of annealing geometries were investigated. While all annealing furnaces were able to form good ohmic contacts, comparative analysis suggests that the most optimum configuration appears to be the quartz tube furnace at low temperature and longer holding times. This configuration is also less energy intensive due to its batch processing capability. Conventional IR RTA furnace is only slightly lower in terms of performance. The radial furnace has lower temperature capability and has the potential to be comparable to quartz furnace increased power.

4.7 Silver Contact Variation with Annealing Configurations

The principal objective of annealing experiments is to determine an optimum energy-conserving approach to lowest resistance ohmic contact between Ag and n/p Si wafer with emitter R_{SH} of ~ 50 Ω/square. This study will help enhance physical understanding of Ag/Si contact formation. In all measurements in the following sections, R_T vs distance data is plotted to extract R_C, ρ_C, R_{SH}, and L_T parameters; these parameters are subsequently plotted as a function of temperature.

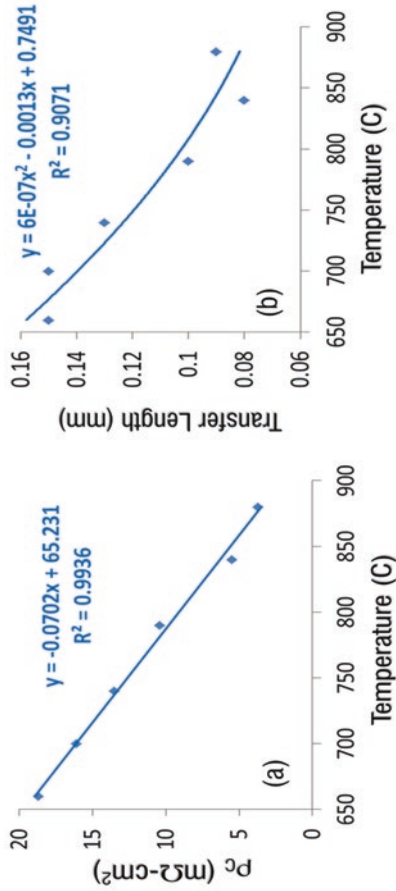

Fig. 4.31 Contact resistivity (**a**) and transfer length (**b**) variations with temperature in parallel-plate rapid thermal annealing furnace

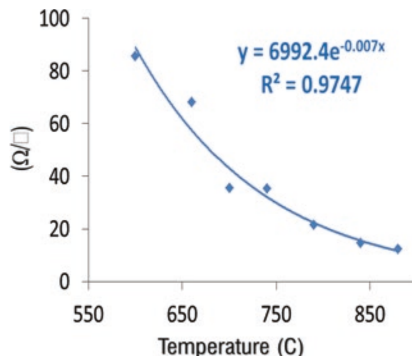

Fig. 4.32 Measured sheet resistance plotted as a function of temperature in parallel RTA furnace

Table 4.9 Al sheet resistance measurements in parallel-plate furnace

Anneal time (sec)	Voltage (mV)	Current (mA)	R_{SH} Ω/square
60	35	2.13	74.4
75	48	3.92	55.5
90	39	4.94	35.8
360	24	7.76	14

4.7.1 Ag/Si Contact in Radial Furnace

In radial furnace, vertically oriented wafers are stationary with halogen quartz lamps serving as heating source. Resistance data as a function of distance is acquired based on thermal profile described in Fig. 4.16. Figure 4.33 plots R_T response for three temperature profiles. It is observed that at low temperature, low contact resistivity of ~ 1.3 Ω/square is achievable. At higher temperatures, contact resistivity increases along with calculated R_{SH} values.

4.7.2 Ag/Si Contact in Quartz Tube Furnace

In quartz furnace, vertically oriented wafers slowly travel along a virtual six-zone temperature profile (Fig. 4.15) with resistive heaters serving as heating source. A more detailed study on formation of Ag/Si contacts in this furnace has been reported elsewhere [11]; representative data is presented for high and low temperature profiles. Figure 4.34 plots R_T variations with distance for low (700/700/700) and high (600/600/875) temperature annealing profiles; insets provide calculated ρ_C, L_T, and R_{SH} values. It is observed that contact resistivity is high at both temperatures. In order to compare with measured R_{SH} values, Ag films were etched off in HNO_3/H_2O (1:1) solution at room temperature. Figure 4.35 and Table 4.10 present R_{SH} measurements for temperature profiles. For the shallow 50 Ω/square emitters, the increase in R_{SH} is linear with temperature (Fig. 4.35). Therefore, as temperature increases, increasing quantities of Si are incorporated in the Ag film leaving behind higher

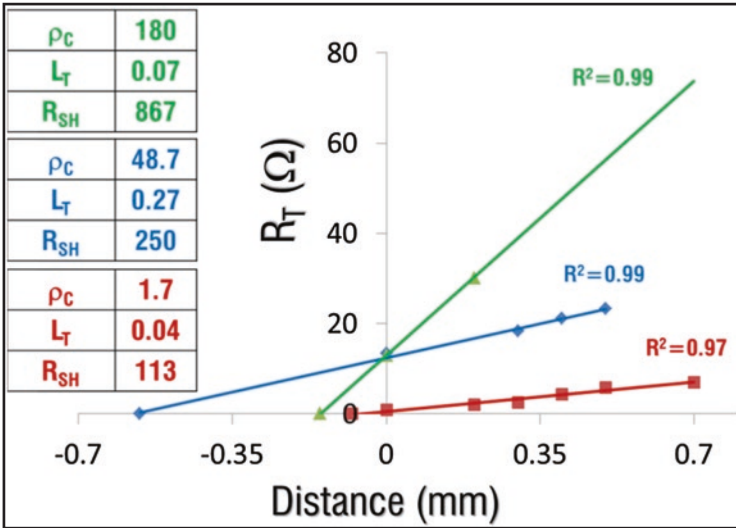

Fig. 4.33 Measured Ag R_T plotted as a function of distance for three annealing times; insets show calculated ρ_C, L_T, and R_C values

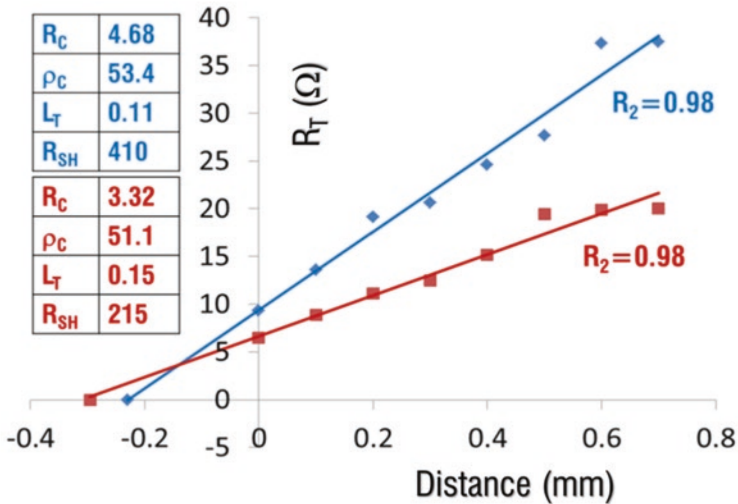

Fig. 4.34 Measured Ag R_T as a function of distance for 700/700/700 (blue line) and 600/600/875 (red line) temperature profiles, for 30-s and 10-s anneal times; insets show calculated ρ_C, L_T, and R_C values

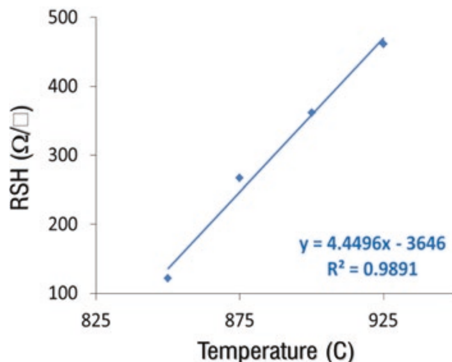

Fig. 4.35 Measured sheet resistance after Ag removal in conventional quartz tube furnace for temperature profiles described in Fig. 4.16

Table 4.10 Ag sheet resistance measurements in quartz tube furnace

Anneal profile	Voltage (mV)	Current (mA)	R_{SH} Ω/square
650/650/650 (45 s)	93	4.2	100.3
600-600-875 (10 s)	110	1.94	256.9
600-600-925 (0 s)	122	1.5	368.4
600-600-925 (10 s)	125	1.19	475.8

sheet-resistant layer with high ρ_C values. This behavior is supported by the four-point data in Table 4.10, and good agreement is observed between measured and calculated R_{SH} values. In this case, Ag/Si contact resistivity behaves conversely to that of Al/Si interface; higher temperature results in higher resistance due to high R_{SH}.

4.7.3 *Ag/Si Contact in Conveyor Belt Furnace*

In conveyor belt RTA, the wafer in horizontal orientation travels across six-zone temperature profile (Fig. 4.12) with IR lamps serving as heating source. A more detailed study on Ag/Si contact in this furnace has been reported elsewhere [11]; some additional features are presented here. Figure 4.36 plots ρ_C and L_T measurements as a function of temperature. Both exhibit slow linear reduction modeled by fourth-order polynomials. Interesting feature of these measurements is increase in contact resistivity at higher temperatures. This is confirmed by etching Ag films and plotting measured R_{SH} as a function of temperature in Fig. 4.37; Table 4.11 presents measurement parameters. Measured R_{SH} values increase linearly with temperature (Fig. 4.37a); however, calculated values exhibit a broad maximum as a function of temperature (Fig. 4.37b) in contrast with experimental data. The R_{SH} variations in RTA and quartz tube are consistent, yet in contrast with quartz tube, significantly lower contact resistivity is achievable in the former furnace. The ability to rapidly raise and lower temperature appears to be critical in Ag/Si contact formation and may also account for low resistivity observed in the radial furnace.

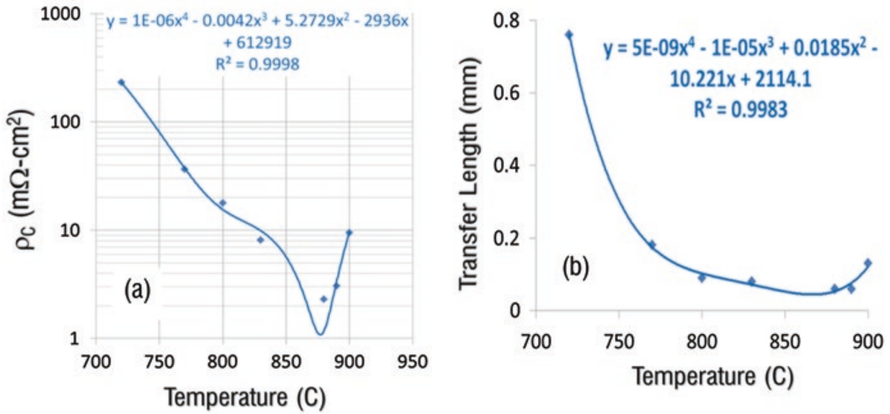

Fig. 4.36 Variations in (**a**) contact resistivity and (**b**) transfer length with temperature in conveyor belt rapid thermal annealing furnace

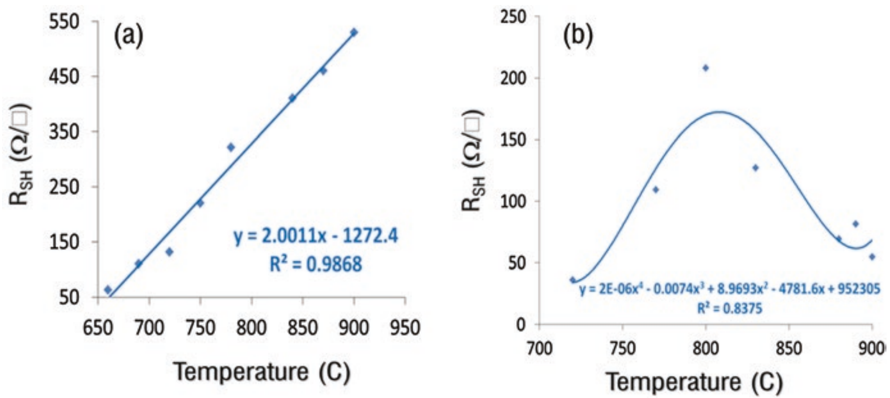

Fig. 4.37 Sheet resistances in conveyor belt RTA furnace configuration: (**a**) after Ag removal and (**b**) calculated from TLM resistance measurements

Table 4.11 Ag sheet resistance measurements in RTA furnace

Anneal temperature (°C)	Voltage (mV)	Current (mA)	R_{SH} Ω/square
660	76	5.3	65
710	92	3.45	120.8
750	106	2.07	232
870	117	1.1	481.8

4.7.4 Ag/Si Contact in Parallel-Plate Furnace

In parallel-plate furnace, the wafer in horizontal orientation is stationary with halogen quartz lamps serving as heating source. Resistance data is acquired as a function of distance with varying thermal profiles (Fig. 4.13b). Figure 4.38 plots calculated ρ_C and L_T values as a function of temperature. Reduction in both parameters can't be curve-fitted with simple mathematical functions. Contact resistivity exhibits a narrow minimum with increasing temperature. At higher temperatures, ρ_C increase is approximately linear. The contact resistivity response appears to be similar to that of the RTA furnace. Figure 4.39 and Table 4.12 provide experimental and calculated R_{SH} measurements. Both exhibit response that can be curve-fitted with

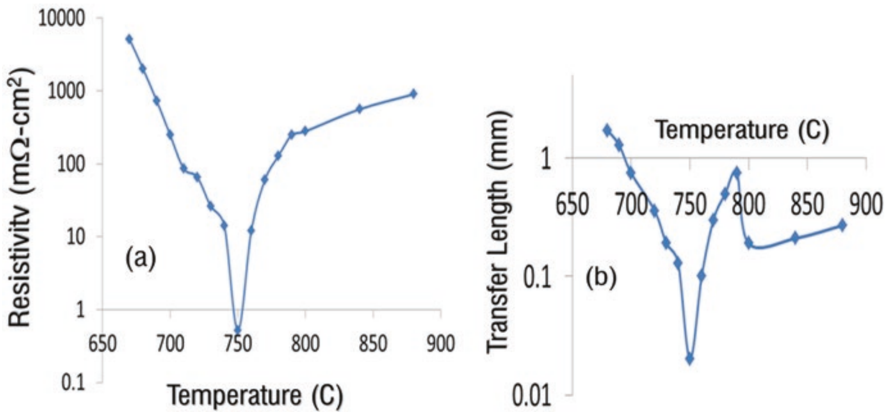

Fig. 4.38 Contact resistivity (**a**) and transfer length (**b**) variations with temperature in parallel-plate rapid thermal annealing furnace

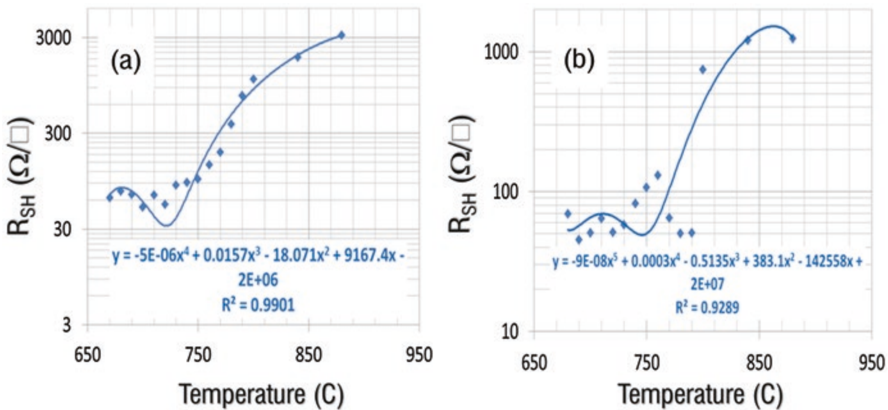

Fig. 4.39 Sheet resistances in parallel-plate furnace configurations after Ag removal (**a**) and calculated from the resistance measurements (**b**)

Table 4.12 Ag sheet resistance measurements in parallel-plate furnace

Anneal time (sec)	Voltage (mV)	Current (mA)	R_{SH} Ω/square
60	78	4.96	71.2
75	110	3.68	135.4
90	123	2.48	224.7
120	158	0.82	872.8

fourth- and fifth-order polynomials. The highest sheet resistance in Table 4.12 starts to approach a current profile similar to that of an n-doped wafer (Table 4.1) except that the voltage increases by ~ 10 and current by ~ 4. Comparison of resistivity response for the RTA and parallel plate reveals many similar features including wide variation in resistivity values and its increase with higher temperature. However, ρ_C values in parallel-plate system are higher and contact formation is a more sensitive function of temperature.

4.7.5 Summary of Ag/Si Contact Formation

Four different types of annealing geometries were investigated. For the Ag/Si contact, parallel-plate furnace response was promising. In contrast with blanket Al/Si contact, Ag contact is formed on Si wafer with about 6% Ag coverage. With large surface transparent to quartz halogen light absorption, wafer temperature is significantly higher than in RTA furnace; therefore, temperature ramp rates during heating and cooling must be faster. The same is true for the radial furnace. Temperature variation in quartz furnace is too slow to form good contacts.

4.8 Morphological Analysis of Al/Si Interface

Morphology of Al/Si regions was characterized with Hitachi field emission scanning electron microscope (FE-SEM) model SU-8230. This SEM features a top detector along with a semi-in type of objective lens and represents advanced version of the upper backscattered electron detector used in earlier S-5500 model. By combining the top detector with the conventional upper detector technology, this SEM provides significant improvement in signal detection system for optimum contrast visualization of signals of secondary electrons, low-angle backscattered electrons, and high-angle backscattered electrons generated from the sample. For characterization purposes, all samples were cleaved and mounted on 45-deg stage to enable cross-sectional imaging. For most of the SEM imaging work, accelerating voltage was in 6–10-kV range and the working distance in 18–20-mm range.

4.8.1 Microstructural Analysis of RTA-Annealed Interface

Figure 4.40 illustrates contact schematic and low-resolution cross-sectional SEM image of the screen-printed Al paste/Si interface after drying. The pre-annealed paste consists mainly of Al spheres with diameter varying over a broad range (~ 0.5 μm to 10 μm); some irregular ellipsoidal shapes are also observed; overall paste thickness is 40 μm. Figure 4.41 displays cross-sectional SEM images of Al/Si interface following RTA annealing in 640–900 °C temperature range. At 640 °C (Fig. 4.41a), the Al/Si interface appears similar to un-annealed interface (Fig. 4.40b) with sphere diameters in 0.7–6-μm range; there is no evidence of Al/Si alloyed interface; contact resistance is too high to measure. At 670 °C (Fig. 4.41b), higher magnification view of the Al/Si interface reveals an alloyed, nonuniform Al/Si thin (~ 0.3 μm) film. For this structure, contact resistance is still high but measurable. At 800 °C (Fig. 4.41c), a thick (~ 4 μm) nonuniform Al/Si film is observed with Al spheres varying in diameter in ~ 0.2–5-μm range; contact resistance at this temperature is ~ 40 mΩ-cm^2. At 900 °C (Fig. 4.41d), a relatively uniform 2-μm-thick Al/Si alloyed film is observed with Al spheres varying in diameter in ~ 0.2–5-μm range; contact resistance at this temperature is approximately 10 mΩ-cm^2. The morphology of the contact interface changes significantly with temperature. At temperatures lower than 670 °C, the Al paste is mostly in the form of intimately connected spheres with diameters in ~ 0.2–5-μm range in the absence of well-defined Al/Si alloyed interface. As temperatures are increased beyond 670 °C, Al/Si alloyed layers of variable and nonuniform thickness are formed. The Al paste structural morphology remains invariant; resistance reduction appears to be a function of the uniformity and thickness of Al/Si alloyed layer. The yellow lines in SEM images indicate direction of elemental concentration scans that will be discussed in the next section.

Fig. 4.40 Pictures of cross-sectional diagram of screen-printed TLM pattern on p-doped Si wafer (**a**) and low-resolution SEM image of screen-printed Al paste after drying at 100 °C for 10 min (**b**)

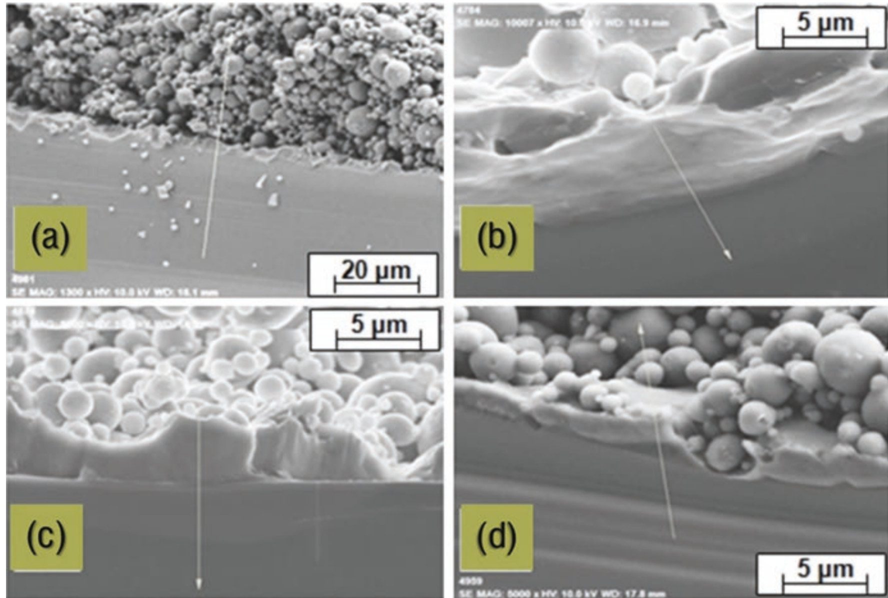

Fig. 4.41 Cross-sectional SEM images of Al/Si interface following annealing at 640 °C (**a**), 670 °C (**b**), 800 °C (**c**), and 900 °C (**d**) in conveyor belt RTA furnace

4.8.2 Microstructural Analysis of Quartz Furnace-Annealed Interface

Figure 4.42 displays cross-sectional SEM image of Al/Si interface following quartz furnace annealing at 850 °C. Figure 4.42a illustrates nonuniform Al/Si alloyed region of ~ 1.5-µm maximum thickness below interconnected Al spheres with diameters in ~ 0.5–3-µm range. Figure 4.42b shows cross- sectional SEM image of the Al/Si interface annealed at 925 °C. A nonuniform Al/Si alloyed region of ~ 1.4-µm maximum thickness is formed below interconnected Al spheres with diameters in ~ 0.25–3-µm range. Despite structurally similarity of Al/Si interfaces, there is an order of magnitude reduction in resistivity for 75 °C temperature change.

4.8.3 Compositional Analysis of Annealed Interface

Compositional analysis of the metal contact interface regions was carried out with the Hitachi SU-8320 FE-SEM. This FE-SEM is equipped with high-resolution detection system of characteristic X-rays generated by samples under electron beam irradiation. The elemental detection system was based on energy-dispersive X-ray spectrometer (EDX) consisting of a solid-state detector (Si (Li)) in combination with multichannel pulse height analyzer and host of advanced data processing systems. EDX measurements were focused on detection of Si, Al, Ag, and oxygen. For

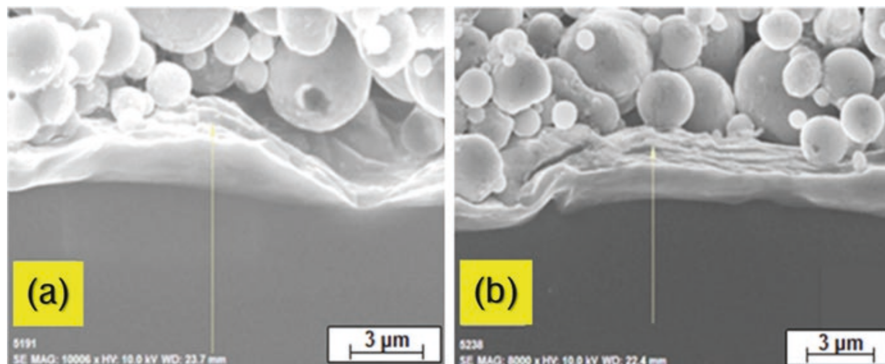

Fig. 4.42 Cross-sectional SEM images of quartz furnace-annealed Al/Si interfaces at 850 °C (**a**) and 925 °C (**b**) temperatures

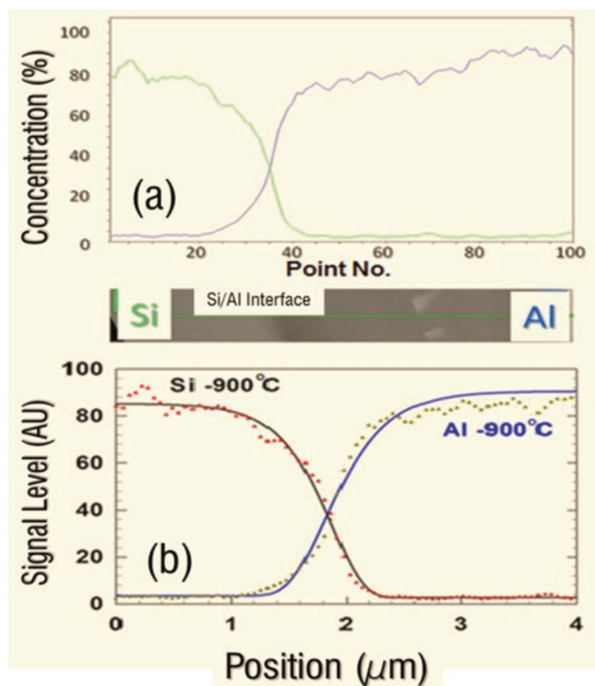

Fig. 4.43 Experimentally observed variations of Al and Si concentrations across the Al/Si alloyed region at 900 °C (**a**) along with nonlinear dynamic curve fitting (**b**); solid lines (black and blue) represent curve fits to the experimental points (green and red triangles)

all measurements, samples were mounted on 45-deg stage at a working distance of 20 mm and accelerating voltage of 10 kV; data was averaged for 30 s. Cross-sectional elemental concentrations were detected across the metal/Si interface at 90°. Figure 4.43a plots a typical line scan measurement of RTA-annealed Al/Si interface at 900 °C. Across interface region of 4-μm length, 100 locations were

tested resulting in position resolution of ~ 0.04 μm; SEM image with green line indicates the scan direction from Si substrate towards Al paste. The plotted data displays Si and Al concentration gradients across the interface region. The concentrations of Si and Al are highest deep in the wafer and paste regions, respectively. In order to accurately measure the width of the contact interface regions, measured data was curve-fitted with nonlinear regression based on sigmoidal, Gompertz [13], and four-parameter equation given by

$$f(x) = y_o + a \times \exp\left(-\exp\left(-(x - x_o)/b\right)\right) \quad (4.31)$$

where the minimum value of parameters a, b, x_o, and y_o were −97.7187, −0.8924, −1.8525, and −2.2813, respectively; the maximum values were 293.1561, 2.6771, 5.5575, and 6.8439, respectively. Figure 4.43b plots the experimental data along with the nonlinear fit; excellent agreement is observed. All subsequent EDX measurements were curve-fitted with this routine and achieved convergence of 99.5%.

Figure 4.44a plots the curve-fitted concentration variations for conveyor belt RTA-annealed contacts. While the Al concentration slopes appear identical across the interface region at both the lowest (640 °C) and the highest (900 °C) temperatures, Si slopes are significantly different. The widths of the interface regions

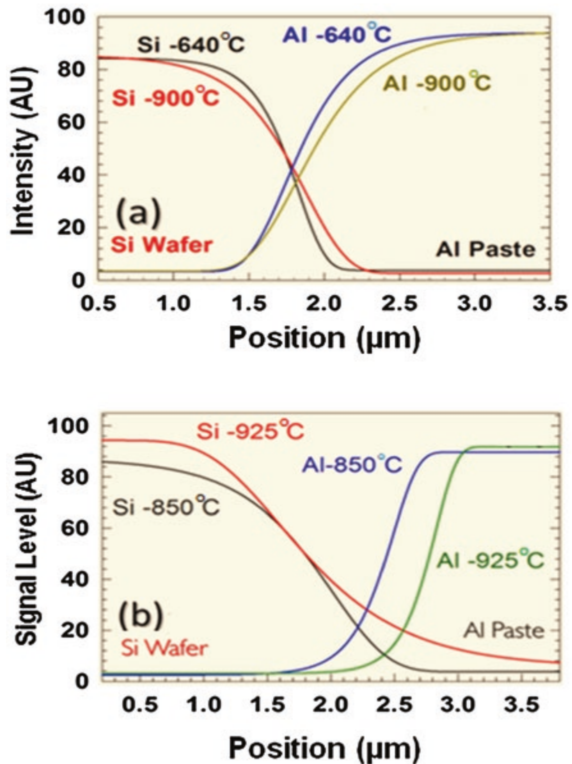

Fig. 4.44 Al and Si concentrations plotted as a function of distance for contacts formed in RTA (**a**) and quartz (**b**) furnaces

Table 4.13 Widths of interface regions for RTA and QTF configurations

Temperature and configuration	Al/Si width (μm)
640 °C/RTA	0.8
850 °C/quartz tube	1.2
900 °C/RTA	1.0
925 °C/quartz tube	1.8

measured at the bottom part of each graph have been listed in Table 4.13. The Al/Si contact region width increases by 25% as temperature is increased by 40%. Figure 4.44b plots the curve-fitted concentration variations for vertically annealed contacts in quartz tube furnace. The slopes of Al appear identical across the interface region at both the lowest (850 °C) and the highest (925 °C) temperatures. Si slopes are significantly different in comparison with the horizontal annealing configuration. The widths of the interface regions measured at the bottom part of each graph have been listed in Table 4.13. The Al/Si contact region width increases by 350% as temperature is increased by 9%.

Composition of Al paste has been investigated. An interesting feature was detection of Si films across the entire width of the paste region. Below 700 °C, Si presence inside the paste was negligible. Figure 4.45 displays SEM images of Si films near the Si substrate (Fig. 4.45a) and middle of the paste (Fig. 4.45b) along with respective Al/Si concentration variations in Figs. 4.45c and d; the green line on the SEM image below the plotted data indicates scan direction across the Al/Si structures. Almost symmetric correlation in concentration variation is observed with dark and white regions corresponding to Si and Al, respectively. Colored contrast maps of elemental concentrations in Fig. 4.46 illustrate this more vividly; the black and white SEM image represents the profile for which colored contrast elemental concentrations were measured. The green regional map of Al concentration reveals a dark region without Al. The yellow regional map of Si reveals its highest concentration in the dark, Al-free region. The red regional map of O concentration reveals its highest concentration in Al-rich regions. These regions likely represent thin Al_2O_3 films formed on the surface of Al. The visual information presented in Fig. 4.46 is insightful; however, it fails to provide quantitative information. Finite area EDX scans were carried out in Al and Si regions in order to precisely determine surface concentrations. Figure 4.47 displays SEM images of Al/Si composite spheres of diameter ~ 1.5 μm. The yellow rectangular area in the dark region for Si (Fig. 4.47a) and the light region for Al (Fig. 4.47b) identify regions selected for EDX measurements. The dark region reveals ~ 2.75 times higher Si concentration than Al along with ~ 4.5% concentration of oxygen (Fig. 4.47c). In contrast, the light region reveals twice as much Al concentration than Si along with ~ 9% concentration of oxygen (Fig. 4.47d). The higher O concentration in the light region likely related to formation of Al_2O_3 and SiO_2 films. This type of composite structure was observed in almost all of the Al paste irrespective of its location either near the Si/Al or Al/Air interface.

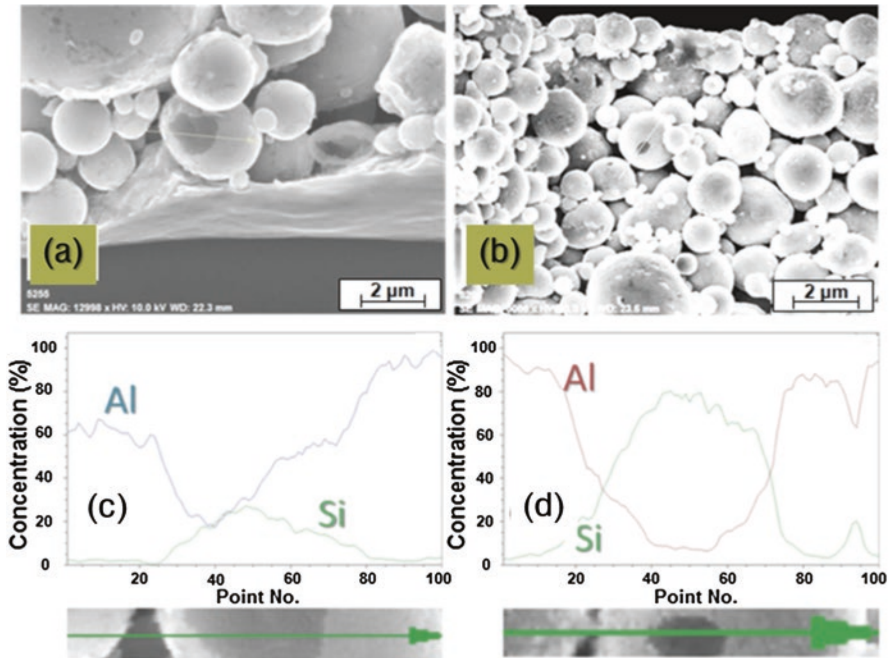

Fig. 4.45 SEM images of Si films in Al paste near the Si substrate (**a**) and closer to the Al/air interface (**b**) along with their respective concentrations near the Si substrate (**c**) and near the Al/air interface (**d**); SEM images of the linescans across the Al/Si interfaces are also included for clarity

4.8.4 Contact Formation Mechanisms

Aluminum screen-printed contact formation using rapid thermal annealing has been extensively investigated in terms of process parameters, microstructure, composition, and inter-diffusion of Al and Si; a detailed summary is provided in references [14–24]. Generally agreed consensus is that as temperature is increased above the melting point of Al (~ 660 °C), Al starts to melt and individual micrometer-sized spherical particles form metallurgical contact with each other. At the same time, Si starts to diffuse into Al with increasing concentrations. These processes continue until the temperature reaches its highest point and cool down is initiated. As temperature is reduced and Al begins to solidify, Si concentration in Al is reduced to ~ 12.6% at its eutectic point (577 °C). During this cool down phase, Si is diffused out of solid Al and epitaxially grows on the underlying Si substrate with significantly reduced Al concentrations based on its solid solubility limit. Most of the published work relates to various aspects of physical mechanisms underlying the Al/Si contact. There is lack of comprehensive investigation on correlated model incorporating electrical, thermal (time and temperature), structural, and compositional aspects of the A/Si contact.

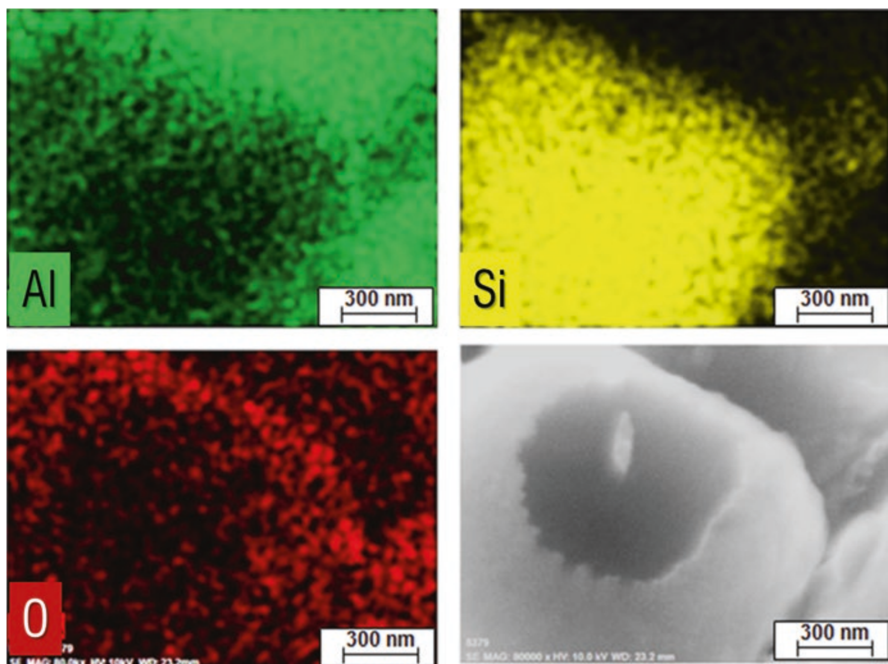

Fig. 4.46 Colored secondary-electron images of Al, Si, and O concentrations for the SEM profile (bottom right)

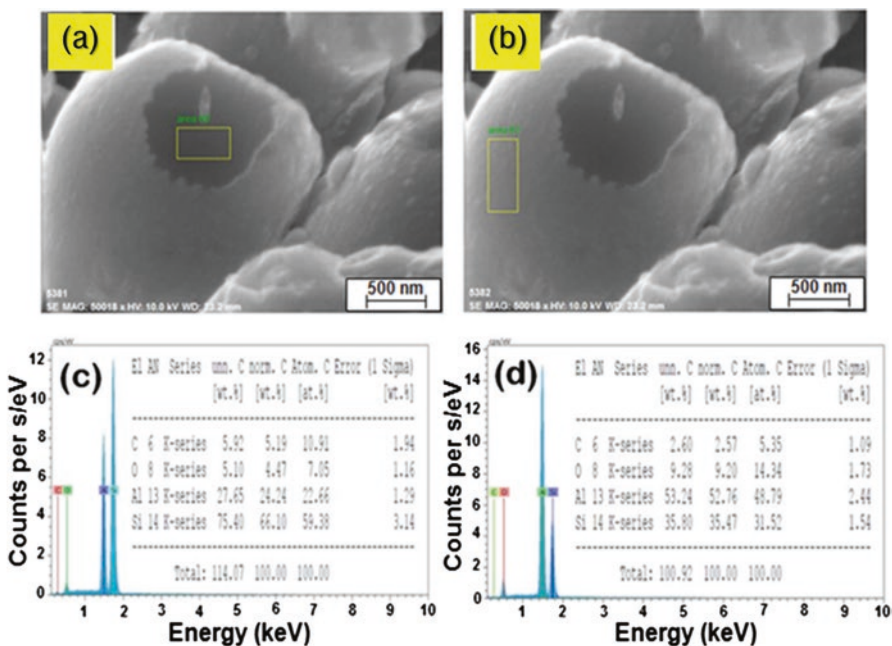

Fig. 4.47 SEM images of sintered Al/Si spheres annealed at 900 °C with dark (**a**) and light (**b**) regions along with their respective EDX analysis (**c** and **d**)

The work presented here is an attempt at further clarification. Figure 4.48 displays SEM image of annealed contact at 900 °C in which four distinct regions can be identified: (a) the sintered Al/Si spherical particles, (b) Al/Si eutectic layer, (c) epitaxial BSF layer, and (d) silicon substrate. These regions will be explored in more detail in order to develop a compact model of the Al/Si screen-printed interface contact. The yellow rectangular region (Fig. 4.48a) identifies the location and the spot area for a series of finite areas EDX composition scans from the Si substrate to the top of the Al/Si eutectic region. Curve-fitted concentrations of Al and Si (Fig. 4.48b) and O (Fig. 4.48c) from the top of Al/Si eutectic to the Si substrate correspond to depth variation of ~ 7 μm. The Al/Si eutectic region exhibits rapid reduction in Al concentration from its maximum value to ~ 12%. Immediately below the eutectic layer lies the Al-doped Si region which consists of two parts: the epitaxial layer and the Si substrate; the width of the entire Al-doped region is ~ 4 μm. The width of the Al-doped epitaxial layer, identified by its contrast in Fig. 4.48a, is approximately 2 μm. It is also identifiable through the variation in O concentration (Fig. 4.48c). The O concentration varies by a factor of 3 indicating some growth of Al_2O_3 and SiO_2 during the cooling down phase, since in pure Si substrate, O concentration inside Si is below the resolution limit of the EDX measurement system employed here. The widths of the Al-doped region measured in Fig. 4.48 and Table 4.13 are in good agreement with the reported work in literature.

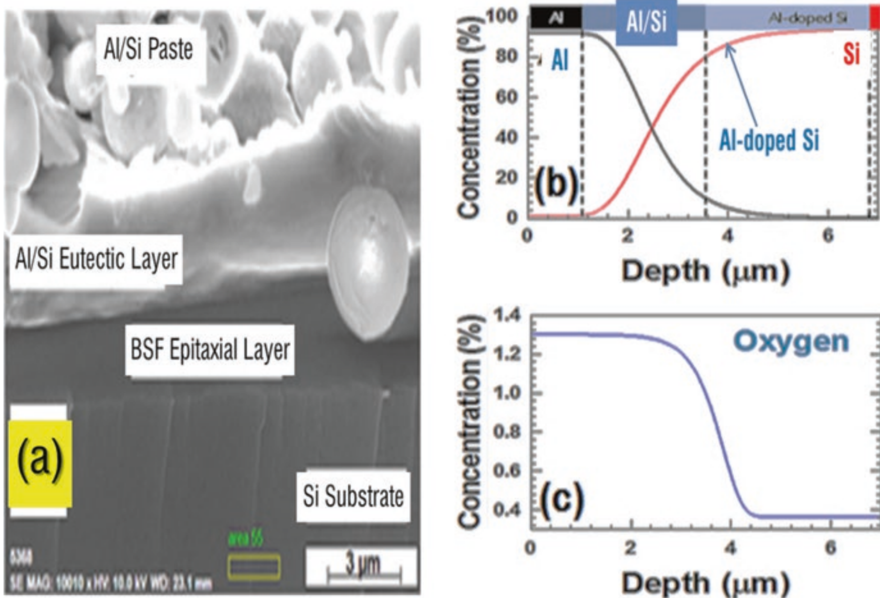

Fig. 4.48 SEM image of screen-printed Al/Si contact annealed at 900 °C (**a**) identifying four different regions from the top to bottom: cured Al/Si paste, Al/Si eutectic region, epitaxially grown Al-doped BSF layer, and Si substrate; (**b**) concentrations of Al and Si across the Al/Si eutectic and Al-doped BSF regions and O concentration across the same regions (**c**)

High Al concentrations as a function of depth can't be explained by diffusion models [25]. Figure 4.49 plots calculated Al diffusivity in Si (Fig. 4.49a) and its concentration variation inside Si as a function of temperature and depth (Fig. 4.49b), respectively; Al-diffusion time was 20 s. Simulations reveal Al diffusivity enhancement by almost six orders of magnitude as temperature is increased from 600 °C to 1000 °C. In contrast, even for the highest diffusion temperature, Al depth inside Si extends to less than 0.5 µm. Thus, higher Al concentration observed in Fig. 4.48 can only be attributed to epitaxial regrowth of Al-rich Si during cool down phase as excess Si is ejected out of rapidly cooling Al paste. The annealed paste region at the top of Al/Si alloyed region with varying distributions of Si concentrations supports this conclusion.

4.8.5 Resistivity Variation

Lowest contact resistivity was observed with quartz tube annealing. In contrast to the RTA furnaces, heating in quartz tube proceeds in quasi-steady-state fashion. Structural analysis reveals that steady-state heating facilitates formation of thin

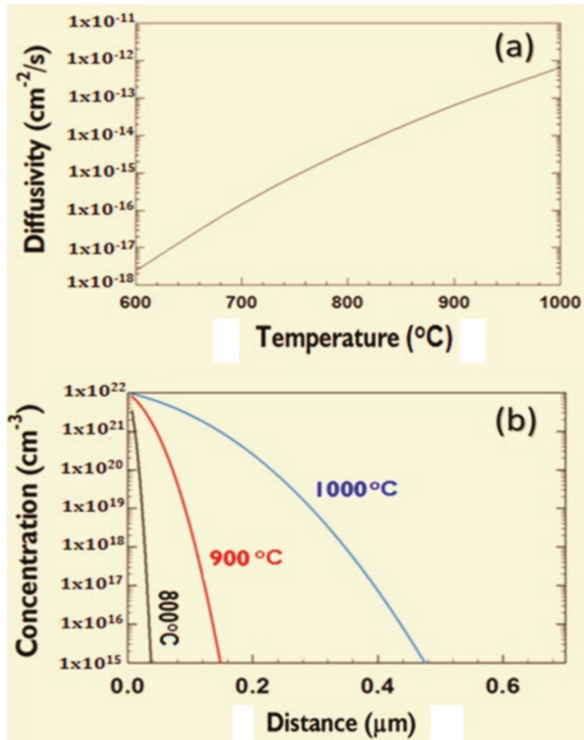

Fig. 4.49 Diffusivity of Al as a function of temperature (**a**) and Al doping concentration variation inside Si substrate at three different temperatures (**b**)

continuous Al/Si films sandwiched between pure Al pastes (Figs. 4.50a and b) enabling reduction in resistance. Slow and steady thermal ramp rates facilitate merging of individual Al spheres into large (~ 20 × 30 μm^2) grains (Fig. 4.50c), which again reduces resistance due to lower density of grain boundaries. The linescan concentration scans (Figs. 4.50d–f) of the SEM images reveal this with better clarity. Silicon distribution across the paste regions is localized and exists uniformly across the entire width of the Al paste.

Based on the measurements and analysis presented above, a phenomenological model of the screen-printed Al/Si interface is presented in Fig. 4.51. Five distinct separate regions are identified and briefly described below.

(i) Sintered paste region consisting of Al/Si spheres with varying shapes and dimensions and Si/Al concentrations. The Al/Si spheres consist of a core of pure Al embedded in thin shells of $Al_2O_3$and SiO_2.
(ii) Voids in the paste and Si/Al interface regions arising from overlaps between spheres of varying diameters.
(iii) Al/Si eutectic region with rapid concentration gradient from paste to substrate.
(iv) Al-doped back surface region consisting of epitaxial layer.
(v) Lightly, Al-doped Si substrate with Al concentration below the resolution limit of EDX.

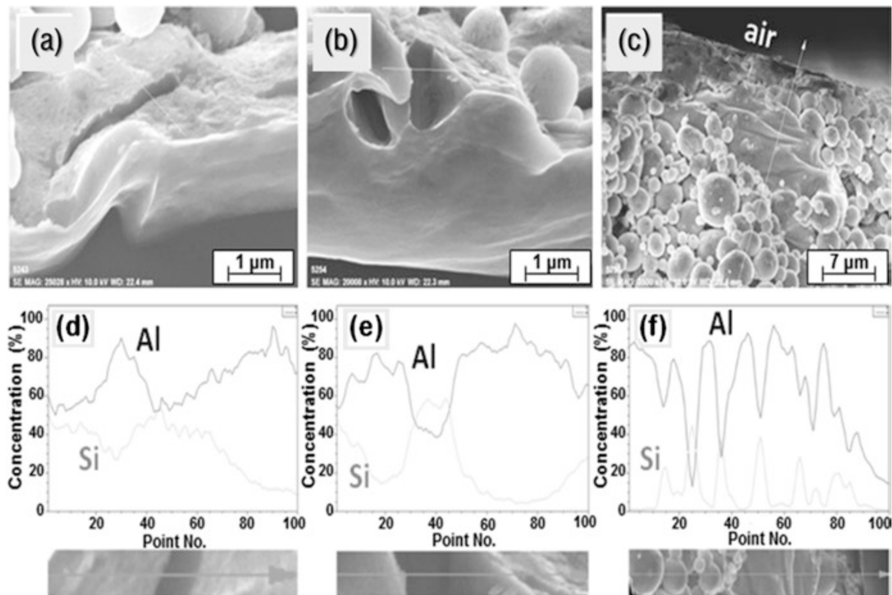

Fig. 4.50 SEM images of Si and Al films embedded within the aluminum paste (**a**, **b**), large Al grains from merging of individual spheres (**c**) along with their respective linescans (**d**–**f**) across the indicated yellow lines; insets with green lines indicate direction of linescans

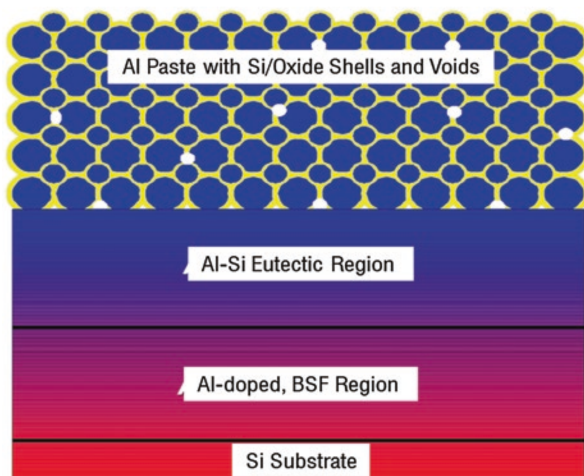

Fig. 4.51 Model of screen-printed Al/Si contact formed by thermal annealing

The width of Al/Si eutectic regions is a strong function of temperature and time. In quartz tube configuration, the wafer spends almost twice as much time in comparison with RTA furnace at a slower rate of temperature change. This type of thermal process leads to more uniform Al/Si eutectic regions with larger thicknesses and lower sheet resistances.

4.8.6 Summary of Al/Si Interface

Key feature of the Al/Si contact interface relates to thermal ramp rate. The rate of cooling down, in particular, has a significant impact on epitaxially grown Al-doped films. If the rate of thermal change is too fast, the eutectic region is likely to consist of higher Si concentration since some of melted Si will be sandwiched between Al pastes. Figure 4.52 clearly illustrates this in the RTA-annealed Al paste at 900 °C peak firing temperature. The SEM and concentration scan measurements of Al/Si interface exhibit a eutectic region with trapped sub-μm Si crystallites with some of them extending to the interface. The presence of such structures supports the proposed model in terms of growth mechanisms as well as increased resistivity. Longer time duration enables formation of uniform Al-doped epitaxial layers below Al/Si eutectic region.

4.9 Morphological Analysis of Ag/Si Interface

A physical model of the Ag/Si contact interface based on extensive morphological and compositional analysis is presented.

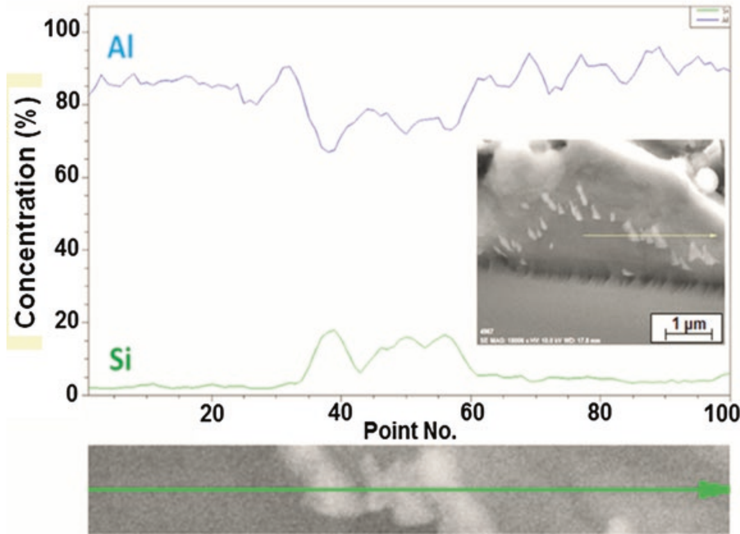

Fig. 4.52 SEM image of the annealed Al paste/Si interface exhibiting eutectic region (**a**) and its elemental EDX analysis (**b**)

4.9.1 Microstructural Analysis of RTA-Annealed Interface

Figure 4.53 displays cross-sectional schematic view of Ag/Si contact interface (Fig. 4.53a) and low-resolution SEM picture of screen-printed Ag paste (Fig. 4.53b) after drying in air at 150 °C for 10 min. The pre-annealed Ag paste consists of spherical Ag spheres with diameters in ~ 0.1–2-μm range interspersed with randomly distributed PbO_2 and SiO_2 pockets (dark regions in Fig. 4.53b).

For ease of comparison, only samples at lowest and highest temperatures are presented. Figure 4.54 displays cross-sectional low- and high-resolution SEM images of thermally annealed Ag/Si interface at peak temperatures of 640 °C (a and b) and 800 °C (c and d) conveyor belt RTA furnace. At 640 °C temperature, the Ag/Si contact is not uniform across the interface and is interspersed with high density of voids at Si interface (Fig. 4.54a). Higher magnification SEM image (Fig. 4.54b) reveals a continuous Ag/Si alloyed region. The yellow lines in SEM images identify direction and length of electron diffraction elemental detection scans discussed later in this section. At 800 °C temperature, the Ag/Si contact exhibits superior uniformity with negligible distribution of voids (Fig. 4.54c). Higher magnification SEM image (Fig. 4.54d) illustrates emergence of glass films sandwiched between paste and Si substrate as well as Ag-Si alloyed contact; small spherically shaped features are also observed at the interface with Si substrate.

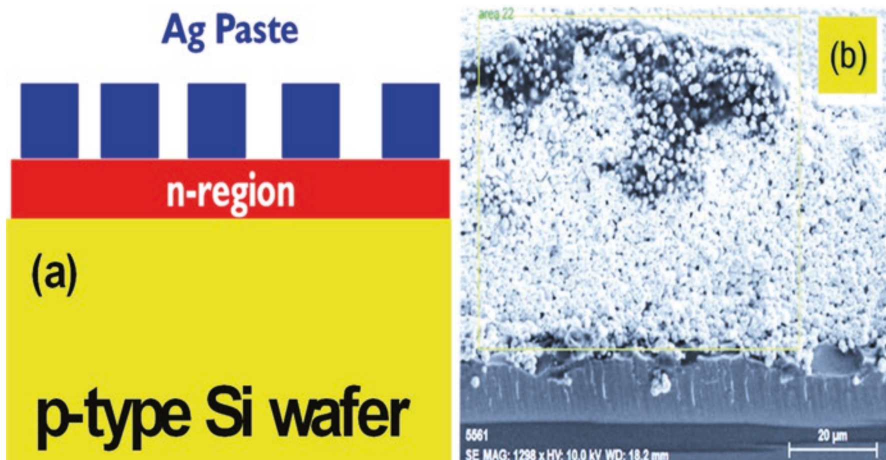

Fig. 4.53 Cross-sectional diagram of the screen-printed TLM pattern on an n-doped Si wafer used in this study (**a**) and low-resolution SEM image of screen-printed silver paste after drying (**b**)

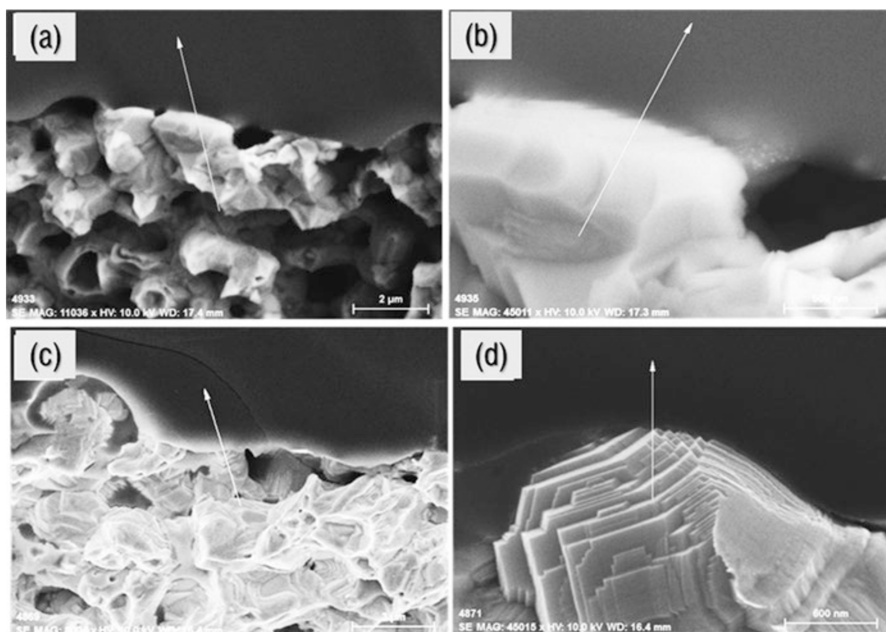

Fig. 4.54 Cross-sectional scanning electron microscope (SEM) images at low and high resolutions of Ag/Si alloyed contact interfaces at 640 °C (**a**, **b**) and 800 °C (**c**, **d**); yellow lines indicate linescan

4.9.2 *Microstructural Analysis of Quartz Furnace-Annealed Interface*

Figure 4.55 displays low- and high-resolution cross-sectional SEM images of Ag/Si contact interface annealed at 850 °C and 925 °C in quartz tube furnace. At 850 °C, the Ag/Si contact is mostly uniform with vastly reduced void density (Fig. 4.55a) in contrast with the 640 °C horizontal RTA contact. The Ag paste is sintered uniformly with larger-sized islands intimately connected to each other. Higher magnification SEM image (Fig. 4.55b) reveals presence of thin glass regions sandwiched between Ag paste and Si interface. At 925 °C, the Ag/Si interface consists mainly of regions with empty spaces (voids) and with glass film (Fig. 4.55c). At the interface with Si substrate, Ag paste appears to make contact through the glass film (Fig. 4.55d). The thickness of Ag/glass/Si alloyed region varies broadly, and presence of small spherically shaped features at Si substrate is also observed (Fig. 4.55d).

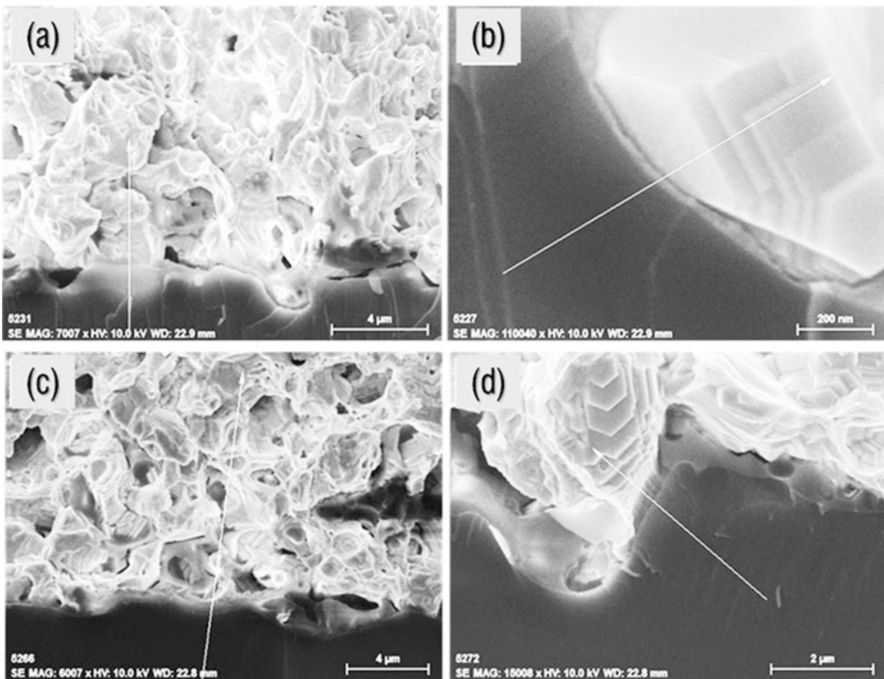

Fig. 4.55 Cross-sectional SEM images at low (**a**) and high (**b**) resolutions of Ag/Si alloyed contact interfaces at 850 °C (**a**, **b**) and 925 °C (**c**, **d**) in quartz furnace; yellow lines indicate linescans

4.9.3 Compositional Analysis of Annealed Interface

Compositional analysis of the metal contact interface regions is carried out with the Hitachi SU-8320 FE-SEM; details have been described in Section 4.9. In accordance with linescan locations identified in SEM images (Figs. 4.54 and 4.55), Ag and Si elements were detected across the contact interface. Figure 4.56 plots a typical linescan measurement for Ag/Si contact annealed at 900 °C. A total of 100 measurements were acquired along the 4.5-μm linescan resulting in position resolution of ~ 0.045 μm. The plotted data (red triangles) describe concentration gradients of both Si and Ag across the interface region. Concentrations of Si and Ag are highest deep in the wafer and paste regions, respectively. In order to accurately measure the width of the Ag/Si interface regions, experimentally measured data was curve-fitted (black line in Fig. 4.56a) with nonlinear regression based on sigmoidal, Gompertz, and four-parameter equation given by

$$f\left(x\right) = y_o + a \times \exp\left(-\exp\left(-\left(x - x_o\right)/b\right)\right) \tag{4.32}$$

where the constants are given by

	Minimum	Maximum
a	−26.6881	80.0643
b	−2.8257	0.9419
x_0	−2.5336	7.6008
y_0	−0.3551	1.0654

The experimental data (red triangles) plotted in Fig. 4.56a along with the nonlinear fit (black line) are in excellent agreement. In all subsequent EDX measurements, curve-fitting was carried out using this process with convergence of 99.5%. This method is applied to determine concentration profiles for all annealing profiles. Figure 4.56b plots concentration gradients of RTA Ag/Si contacts. The Ag

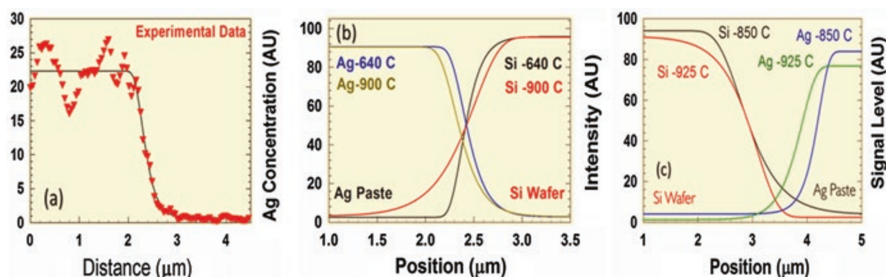

Fig. 4.56 Energy-dispersive X-ray (EDX) linescan analysis of a Ag/Si alloyed contact: red triangles represent experimental data and black line nonlinear fit to the data (**a**), curve-fitted Ag/Si concentration variations at 640 °C and 900 °C in RTA (**b**), and the same in quartz tube configuration at 850 °C and 925 °C (**c**)

Table 4.14 Widths of Ag/Si interface regions in RTA and quartz tube configurations

Temperature/Configuration (°C)	Width (μm)
640/RT A	0.9
850 Quartz Tube	2.4
900/RTA	1.9
925 Quartz Tube	3.1

concentration slopes appear identical across the interface region at both the lowest (640 °C) and the highest (900 °C) temperatures; Si slopes are significantly different. The widths of the interface regions measured at the bottom part of each graph have been listed in Table 4.14. The Ag/Si contact region width increases by a factor of 2 as temperature is increased by a factor of 1.4. Figure 4.56c plots concentration gradients for Ag/Si contacts annealed in the quartz tube furnace. The slopes of Ag appear identical across the interface region at both the lowest (850 °C) and the highest (925 °C) temperatures; Si slopes are significantly different. The widths of the interface regions measured at the top part of each graph have been listed in Table 4.14. The Ag/Si contact region width increases by 1.3 as temperature is increased by a factor of 1.1.

In order to understand the physical mechanisms underlying the Ag/Si contact, it is necessary to examine paste constituents. The composition of commercial silver paste continuously evolves to keep up with evolving solar cell configurations. Figure 4.53b illustrates structural morphology and composition of pre-annealed Ag paste to serve as a baseline for comparison as its morphology and composition vary with temperature. Most significant impacts are detected at highest temperature of 900 °C and have been extensively investigated. Figure 4.57a displays SEM image of Ag/Si interface following RTA process at 900 °C which reveals that the Ag spheres have coalesced to form large-grained (~ several μms) metal films intermixed with empty voids and glass films. Glass films of variable thickness are sandwiched between Ag metal and underlying Si substrate. This process is also accompanied by formation of large "Ag" crystallites distributed within the glass as well as at Si substrate. The EDX analysis of two principal constituent parts, i.e., the Ag paste and glass, was carried out. Figure 4.57b plots EDX measurements of the Ag regions for pre-annealed (black line) and annealed (red line) Ag pastes; concentrations of various elements have been summarized in Table 4.15. It is noted that the compositions are almost identical except for detection of phosphorous (P) signal. Figure 4.57c plots EDX measurements of glass regions for both pre- and post-annealed pastes; concentrations of various elements have been summarized in Table 4.16. Significant differences were observed. At 900 °C, the concentration of Si is increased by almost a factor of 3 and that of Ag reduced by a factor of 5; phosphorus has also been detected. As metal paste is thermally annealed, paste/Si interface structure evolves into the following six distinct regions:

(i) Ag-silicide region.
(ii) Silver paste/glass/Si interface.
(iii) Glass regions within coalesced silver paste.

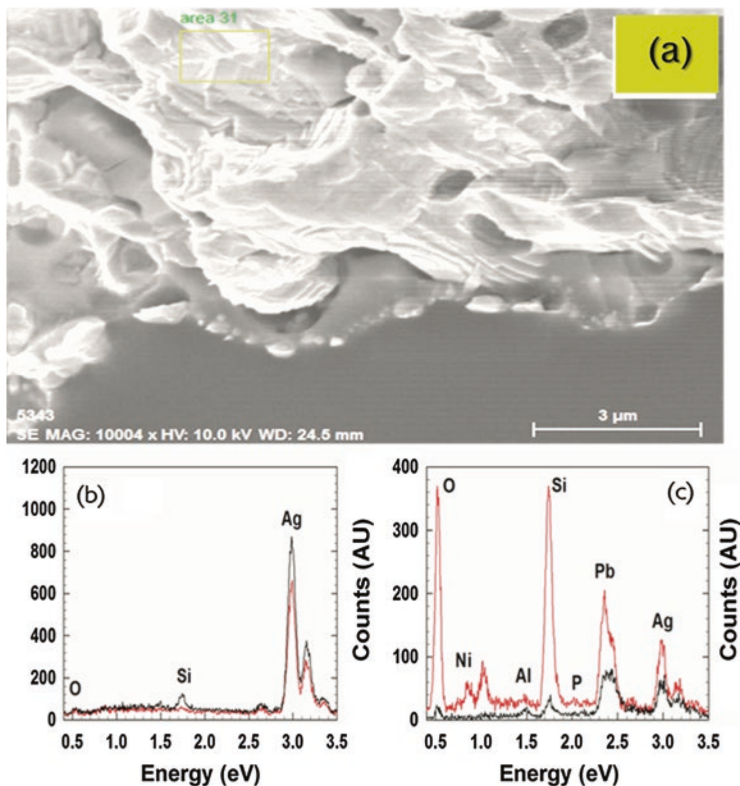

Fig. 4.57 Cross-sectional, low-resolution SEM image of Ag/Si contact annealed at 900 °C (**a**) and its EDX analysis in silver paste region (**b**) and glass regions (**c**) for pre-annealed (black line) and annealed (red lines) cases

Table 4.15 Composition variations in Ag paste at 150 °C and 900 °C

Element	Concentration range at 150 °C (%)	Concentration range at 900 °C (%)
O	~ 1–2	~ 1.5
Si	~ 0.4–6	~ 0.5–3
P	~ 0	~ 0.1–0.6
Pb	~ 0	~ 0
Ag	~ 93–99	~ 97

Table 4.16 Composition variations in glass at 150 °C and 900 °C

Element	Concentration range at 150 °C (%)	Concentration range at 900 °C (%)
O	~ 12–18	~ 12
Si	~ 3–9	~ 26
P	~ 0	~ 0–0.7
Pb	~ 0–60	~ 30
Ag	~ 8–79	~ 15

(iv) Empty voids within coalesced silver paste.
(v) Si films trapped within surfaces of coalesced silver paste.
(vi) Nano- and microscale crystallites randomly distributed within glass and Si substrate interface.

For the sake of simplicity, glass regions (iii) and empty spaces or voids (iv) within the paste can be ignored since their impact on current transport is minimal. The regions in paste critical to low-resistance contact formation include Ag/Si silicide part (i), silver/glass/Si part (ii), Si films in paste (v), and the crystallite structures (vi). The following subsections will provide a detailed analysis of all these regions in order to develop a compact model of the Ag/Si contact.

4.9.4 Phenomenological Model

An extensive, chronological review [26–40] of silver screen-printed contact to n-doped Si substrate reveals a generalized consensus on the following aspects:

(i) Silver paste has two constituents: randomly shaped microscopic Ag particles and glass frit.
(ii) During ramp-up and steady-state thermal processes, glass frit melts and etches silicon nitride anti-reflection film to facilitate contact between Ag and Si.
(iii) During ramp-up and steady-state thermal process, chemical reactions take place to dissolve Ag nanometer (nm)-scale particles in glass frit and deposit on the Si surface.
(iv) During ramp down process, crystalline Si/Ag crystallites are formed at paste/glass/Si interface and glass frit.
(v) Current transport between Ag paste and Si wafer takes place through a combination of multiple mechanisms including tunneling through the glass/Si and glass/Ag crystallites/Si interfaces.

Despite extensive body of work, there is no consensus on how exactly Ag particles are dissolved in glass; how are they crystallized; what are their sizes, geometrical shapes, and compositions; at what temperature they are formed; where are they located; and what is the dominant current transport mechanism? The work presented here develops a coherent phenomenological model of the silver screen-printed contact to explain all of the key features based on reliable and relevant electrical, morphological, and composition data. The phenomenological model developed here is based on the following assumptions:

(i) During ramp-up and steady-state heating, Si diffuses into the glass and silver paste.
(ii) During ramp-up and steady-state heating, silicon and nm-scale Ag particles are intermixed due to their lower melting points.
(iii) During cooling down, excess Si is rejected, some of which is redeposited on the Ag paste.

(iv) During cooling down, a fraction of excess Si forms epitaxial structures with varying Ag and Si concentrations in different sizes and shapes randomly distributed inside the glass film and at Si substrate.

Figure 4.58 represents a schematic diagram of this phenomenological model of the screen-printed Ag/Si contact to the n-doped Si substrate. It identifies several key features such as voids and glass frit in the paste as well as Si (identified as red regions). For ohmic contact, the three distinct regions have been identified and briefly described below.

(i) The alloyed Ag-silicide contact (Region 1) whose specific concentration profiles were described in Figs. 4.56b and c and Table 4.14; for this region, there is virtually no glass film between Ag and Si.
(ii) The metal-insulator-silicon (MIS)-type contact (Region 2) where a glass film is sandwiched between Ag paste and Si substrate; based on process parameters, the glass film may or may not contain nm-scale Ag particles.
(iii) The MIS type of contact (Region 3) in which glass and Ag/Si crystallites are sandwiched between silver paste and silicon substrate.

Synthesis and compositional details of these regions are described below.

4.9.5 Silver Silicide Alloyed Contact

A significant factor in Ag/Si contact formation relates to the abrupt Ag/Si alloyed interface. As part of thermal processing, Ag paste forms an ohmic contact through an alloyed silicide structure with the n-doped surface [41]. The resistivity of this contact is a sensitive function of doping profile, i.e., surface concentration and depth. In this study, doping profile and silver paste were identical; only thermal profiles were varied. Scanning electron microscope profile measurements (Fig.4.54) for RTA configuration reveal Ag/Si interfaces mostly devoid of glass films. In contrast, for the quartz tube configuration at 850–925 °C temperatures, SEM measurements reveal presence of glass films at the interface between paste and Si substrate

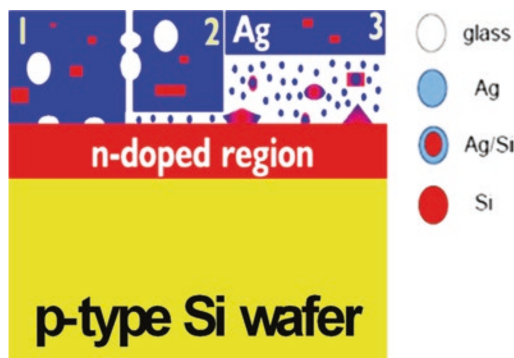

Fig. 4.58 Phenomenological modeling for current transport mechanisms in Ag/Si ohmic contact on n-doped Si substrate

(Fig. 4.55). A comparison of resistivity measurements in RTA and quartz tube configurations reveals the following:

(i) In 640–800 °C temperature range in RTA configuration, resistivity is reduced by three orders of magnitude (Fig. 4.36a).
(ii) In 700–875 °C temperature range in quartz tube configuration, resistivity is invariant (Fig. 4.34).

It appears that Ag/Si silicide contact annealed in quartz furnace exhibits high resistance. The paste/glass/Si interfaces formed in RTA furnace exhibit lower resistance. Higher density of Ag/Si crystallites in RTA-annealed contacts appears to reduce contact resistance. Since silicide based on Ni is far more efficient [42], it is also likely that paste manufacturers incorporate some Ni into paste chemistry since it has been detected through EDX analysis (Fig. 4.57c).

The mechanism of Ag-silicide formation is not clear. Based on diffusion analysis, Ag diffusivity and diffusion profiles can be calculated [43–46]. Figure 4.59a plots Ag diffusivity as a function of temperature in 600–1000 °C range; diffusion time of 60 s was assumed. In temperature range of interest ~ 640–925 °C, diffusivity increases by almost two orders of magnitude. The Ag profiles based on diffusivity calculations, plotted in Fig. 4.59b, exhibit little concentration variation, and its depth inside Si is far less than measured in Figs. 4.56b and c and Table 4.14. The solubility of Ag in Si is also minimal below Ag/Si eutectic temperature of 937 °C. The penetration of metallic impurities has been investigated by Craen et al. in screen-printed solar cells using secondary ion mass spectrometry (SIMS) [47]. Surface concentration levels and penetration depth could not be attributed to diffusion. It appears that migration of Si into Ag paste is mostly responsible for silicide formation.

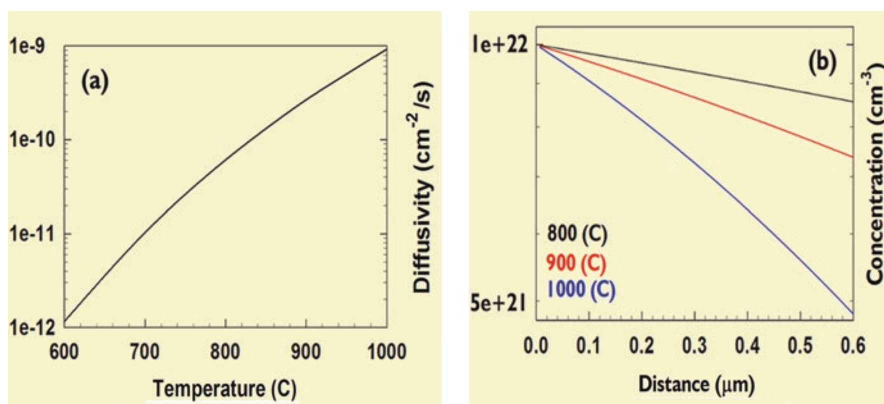

Fig. 4.59 Plots of calculated silver diffusivity (**a**) and its penetration depth (**b**) in Si at three different temperatures

4.9.6 Silicon Diffusion into Silver Paste

In a low (<400 °C) temperature study on metal/Si interfaces, it was observed that Si atoms migrated into metal films at well below their eutectic points [48]. This was attributed to interaction of Si with metals at the interface with <111> crystal orientation as the preferred one. With respect to silver screen-printed contacts in solar cells, the reported work in reference [34] is particularly relevant. SIMS analysis of Si surfaces after metallization reveals reduction in P concentration attributed to Ag/Si alloy formation. In reference [32], intermigration of silicon between substrate and Ag crystallites was observed following forming gas annealing at 475 °C. This loss of Si led to physical gaps between Ag crystals and underlying Si substrate leading to higher contact resistance. Finally, the most recent work in 2017 [41], based on nano-SIMS analysis, reported on almost complete removal of phosphorus from the emitter region. This work also suggests that EDX method is not sensitive enough to detect P, hence the requirement for nano-SIMS. This assumption is in contrast with work presented here in which P has been reliably detected and validates migration of Si film into Ag paste and glass regions.

Detection of elements in EDX is a function of the incident electron energy and electron beam cross-sectional area. In shallow emitters (~ 50 Ω/sq), phosphorous signal detection beyond noise limit (< 0.1%) is difficult. In heavily doped emitters (≈ 20 Ω/sq), phosphorus is reliably detectable over a broad range. Phosphorous signal is even stronger for n-doped SiO_2 films on n-doped wafers. Figure 4.60 plots signal EDX analysis of O, Si, and P from the n-doped SiO_2 films (black line) and Ag/Si structures (red line plot is discussed in the next section). The P signal is well-defined and significantly lower (< 6 x) than that of Si. For SiO_2 films, EDX analysis reveals O signal approximately 1.6 times higher for experimental measurement parameters used in this study. This O/Si concentration ratio is in good agreement with the glass region at 150 °C. Si migration into the paste is likely to be a function

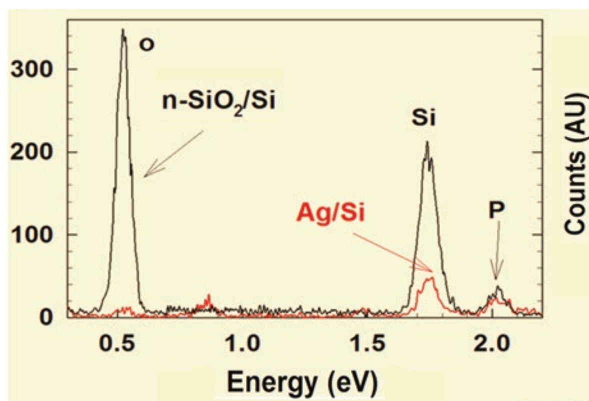

Fig. 4.60 EDX analysis of phosphorous-doped SiO_2/Si interface at normal incidence (black line); red line represents signal from Ag/Si crystallites (discussed later in text)

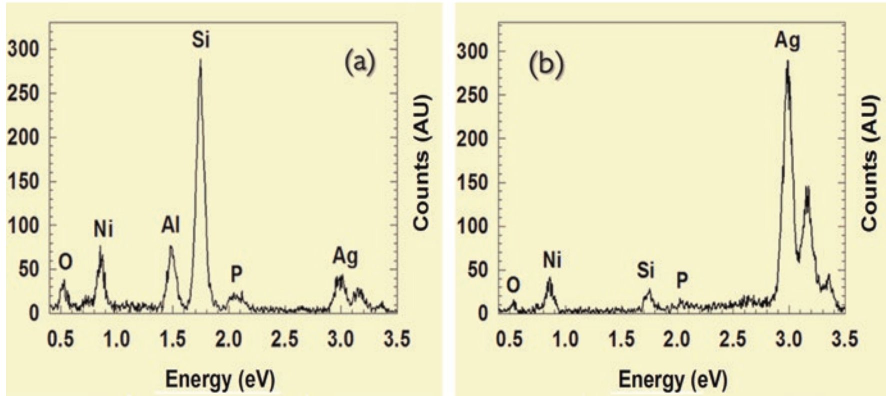

Fig. 4.61 EDX analysis of Si films close to Ag/Si (**a**) and Ag/air (**b**) interfaces

of distance from the paste/Si interface. Figure 4.61 plots EDX analysis of paste regions with significant Si close to Si substrate (Fig. 4.61a) and close to air/paste interface (Fig. 4.61b); concentration ranges have been summarized in Table 4.17. It is noted that Si concentration is significantly higher than O, and the ratio of Si/O varies in approximately 3–5 range. Similarly, P concentration in ~ 0.8–2.5% range is well above the EDX detection limit. Therefore, the signature of Si detected in the paste region is distinct from the SiO_2, and the detection of P from these films is a sufficient proof of Si migration from the doped surface region into the paste. Figure 4.62 plots P concentration as a function of Si (Fig. 4.62a) and Ag (Fig. 4.62b); P concentration is highest at the Ag/Si and lowest at Ag/air interfaces. The increase in Si concentration by a factor of 3 as well as detection of P in glass summarized in Table 4.15 corroborates this migration process. The EDX measurements in Figs. 4.60–4.62 and concentrations in Tables 4.15–4.17 offer convincing proof of P-doped Si film migration into the paste.

4.9.7 Micro- and Nano-Ag/Si Crystallite Growth

During thermal processing (ramp-up and steady-state heating), n-doped Si migrates into Ag paste as the paste itself coalesces and reshapes itself into larger sizes. Simultaneously, glass frit melts and redistributes itself across the paste/Si interfaces. The physical behavior is based on the following chemical reactions:

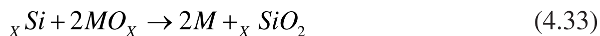

$$ {}_{X}Si + 2MO_{X} \rightarrow 2M + {}_{X}SiO_{2} \tag{4.33} $$

$$ 4Ag + O_{2} \rightarrow 2Ag_{2}O \tag{4.34} $$

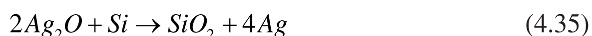

$$ 2Ag_{2}O + Si \rightarrow SiO_{2} + 4Ag \tag{4.35} $$

Table 4.17 Composition variations of constituent components in Ag paste at 900 °C

Element	Concentration range (%)
O	~ 2–9
Si	~ 7–42
P	~ 0.8–2.5
Pb	~ 28–33
Ag	~ 24–89

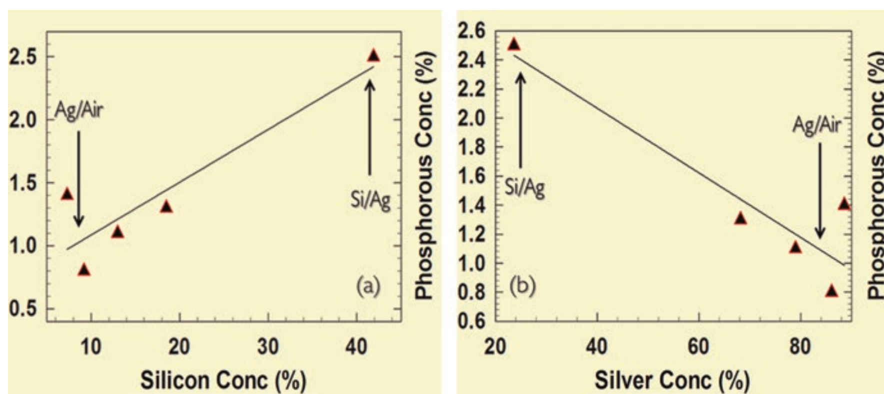

Fig. 4.62 EDX analysis of phosphorous variation as a function of Si (**a**) and Ag (**b**) concentrations in Si films on Ag paste; black line represents linear fit to the experimental data points (red triangles)

Based on findings described above, a simple model for synthesis of "Ag" crystallite structures, illustrated in Fig. 4.63, is proposed. During ramp-up and steady-state heating, extensive intermixing of Ag and Si takes place in liquid state. During ramp-down process, the silver/silicon liquid solution starts to solidify. Lack of Si solubility inside Ag requires excess Si rejection that regrows epitaxially and to a lesser extent oxidizes inside the paste, glass, and substrate regions. Inside the glass and on Si substrate, Ag/Si crystalline structures are formed with varying concentrations. The Ag/Si crystallites broadly vary in dimensions and shapes and are distributed within the glass and on the Si substrate. This hypothesis is supported by relevant work presented here and supported by similar work reported in literature.

The bulk melting points of Ag (961.8 °C) and Si (1414 °C) are far higher than silver paste annealing temperatures. In retrospect, it has been demonstrated that melting points are size-dependent and are substantially lower than their bulk values [49–51]. In reference [49], Au films, deposited on micro- and nanoscale Si structures, were annealed in air under steady-state conditions. In Au/Si microstructures, conventional Au/Si alloyed features were formed. In contrast, in Au/Si nanostructures, crystalline Au spheres embedded in SiO_2 wires were observed. This was attributed to vapor-/liquid-/solid-phase epitaxial growth mechanisms. During steady-state cool down process, excess Si from Au/Si eutectic melt is slowly rejected and converted into SiO_2 nanowires encasing Au spheres. In reference [50], nanoscale

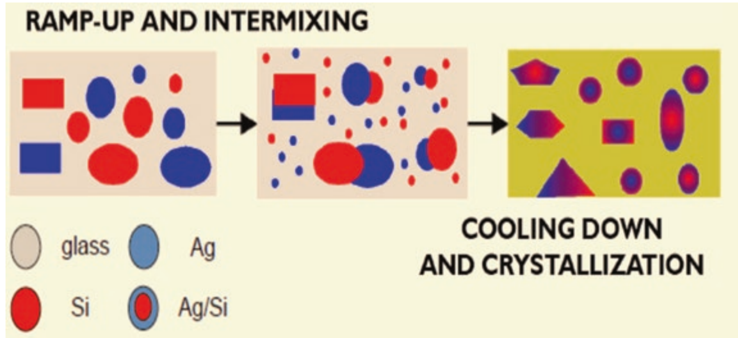

Fig. 4.63 Simplified model for synthesis of Ag/Si crystallites; red regions indicate phosphorous-doped Si and blue regions Ag

Ag films were annealed and their melting points were determined to be as low as 425 °C. In reference [51], growth of Ag nanoscale crystalline structures was reported inside Si under steady-state heating conditions at 750 °C. In silver screen-printed paste formation on solar cells [35], transmission electron microscope analysis revealed formation of an Ag/Si epitaxial superlattice with <111> interface. Silicon atoms were distributed inside the Ag crystalline lattice; density of Si atoms near the surface was negligible. In reference [35], TEM studies only elaborate on epitaxial growth of Ag crystallites inside the glass matrix. The highest temperature during thermal annealing was approximately 750 °C.

Figure 4.64 displays SEM images of glass/Si interface regions with Ag/Si crystallite structures over 640–900 °C temperature range. The Ag/Si crystallites are observed at temperatures as low as 640 °C (Fig. 4.64a); however, these are usually spheres with diameters in ~ 10–100-nm range. The crystallites are distributed within the glass as well as on the Si substrate (Figs. 4.64b and c). When the temperature is increased to 900 °C (Fig. 4.64d), Ag past parameters including density, size, shapes, and distribution are also significantly modified in agreement with the proposed model (Fig. 4.63). Detailed investigation of various Ag/Si crystallites, in order to determine their composition and elemental distribution, is described below.

Figure 4.65 shows EDX elemental mapping of an elliptical-shaped Ag/Si structure formed on the Si substrate; the SEM image is shown as the black/white image at the lower right bottom corner. Elemental mapping indicates that O, P, and Pb are uniformly distributed across the Ag/Si crystallite. The central region of the Ag/Si crystal is dominated by Ag with a slightly higher concentration Ag gradient at the Si interface. Si concentration is minimal at the center and significantly high at the edges. EDX linescan analysis of Ag/Si crystallite parallel (Figs. 4.66a and c) and perpendicular to Si substrate (Figs. 4.66b and d) provides precise compositional information. The highest and lowest concentrations are at the center for Ag (red line) and Si (black line), respectively; at the edges, almost equal Ag/Si concentrations are observed (Fig. 4.66c). The EDX linescan elemental mapping perpendicular to Si substrate (Fig. 4.66d) reveals that the highest and lowest concentrations are

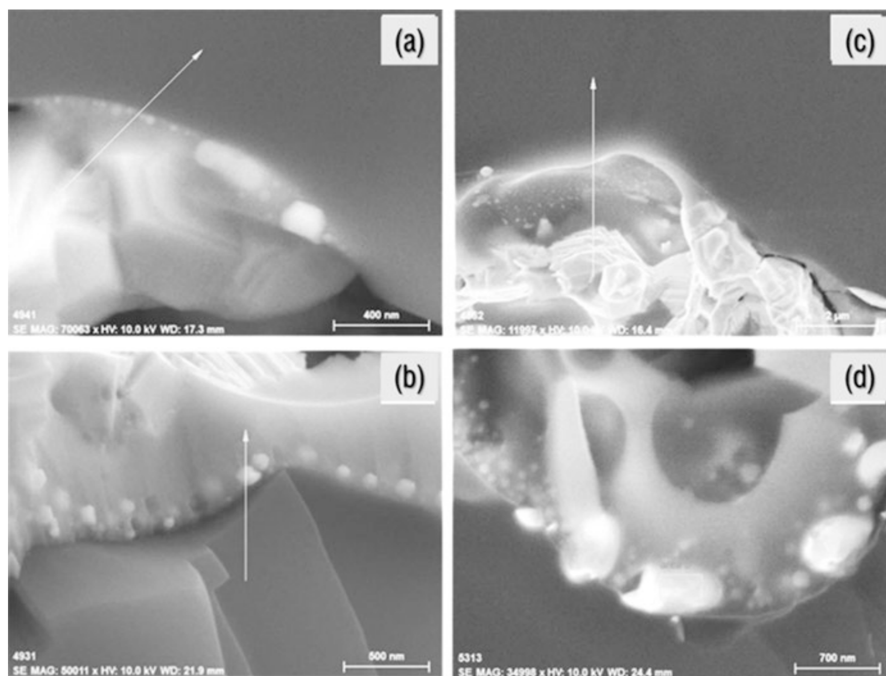

Fig. 4.64 SEM images of the Ag/Si/glass/Si interface regions illustrating widely different geometrical shapes, sizes, and locations of Ag/Si crystallites inside interface glass and at the glass/Si interface over broad temperature range: (**a**) 640 °C, (**b**) 800 °C, (**c**) 860 °C, and (**d**) 900 °C

at the center for Ag (red line) and Si (black line), respectively. At the edges, Ag/Si concentrations, although approximately comparable, appear asymmetric with higher, almost by a factor of 2, concentrations at the Si substrate.

A large number of Ag/Si crystals of varying sizes and shapes were investigated with finite area EDX analysis on account of its higher resolution and sensitivity. No correlation of size with composition was observed. Figure 4.67 plots EDX measurements of three types of crystals with respect to Ag concentrations in Ag/Si crystallites: high (Fig.4.67a), comparable (Fig. 4.67b), and low (Fig. 4.67c); in all cases, O concentration is minimal indicating absence of SiO_2 films; P was also detected. A summary of concentration variations in various Ag/Si crystal structures has been summarized in Table 4.18. Both Si and Ag concentrations vary over a broad range; O concentration range is similar to that observed in glass and Si in glass. Perhaps the most significant finding is enhancement in P signal by a factor of 2 in comparison with Si in Ag paste. The variation in P as a function of Si (Fig. 4.68a) and Ag (Fig. 4.68b) concentrations reveals that P increases linearly with Si and decreases in the same manner with Ag. Since almost all Ag/Si crystals are located within close proximity of Si interface, P concentration is expected to be higher than for Si located further away from Si interface.

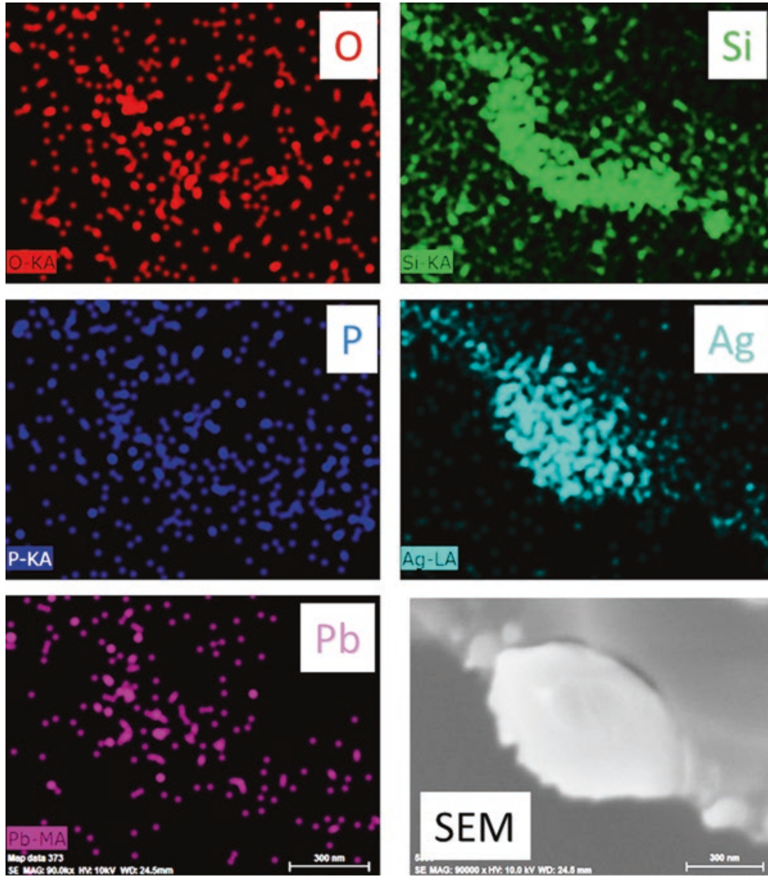

Fig. 4.65 EDX concentration maps of Ag, Si, P, O, and Pb of the Ag/Si crystallite at glass/Si substrate interface whose SEM image is shown in the bottom right picture; annealing was done at 900 °C in RTA configuration

4.9.8 Resistivity Variation with Glass Composition

Contact resistivity is significantly lower in RTA furnace in comparison with the quartz tube configuration. SEM and EDX measurements of contact interfaces in both configurations suggest critical role of Ag/Si crystalline structures inside the glass matrix. The lowest resistivity contacts are for Ag/composite glass with Ag/Si crystals/Si interfaces. The density of Ag/Si crystals and the thickness of the glass layer significantly influence the contact resistivity. This effect has been investigated for thick and thin glass films. Figure 4.69 plots EDX linescan mapping of Ag (red line in Fig. 4.69c) and Si (black line in Figs. 4.69c) concentrations across a thick (~ 1.5 μm) glass film sandwiched between the paste and Si substrate (Fig. 4.69a) in RTA configuration. It is observed that the concentration of Ag is negligible inside

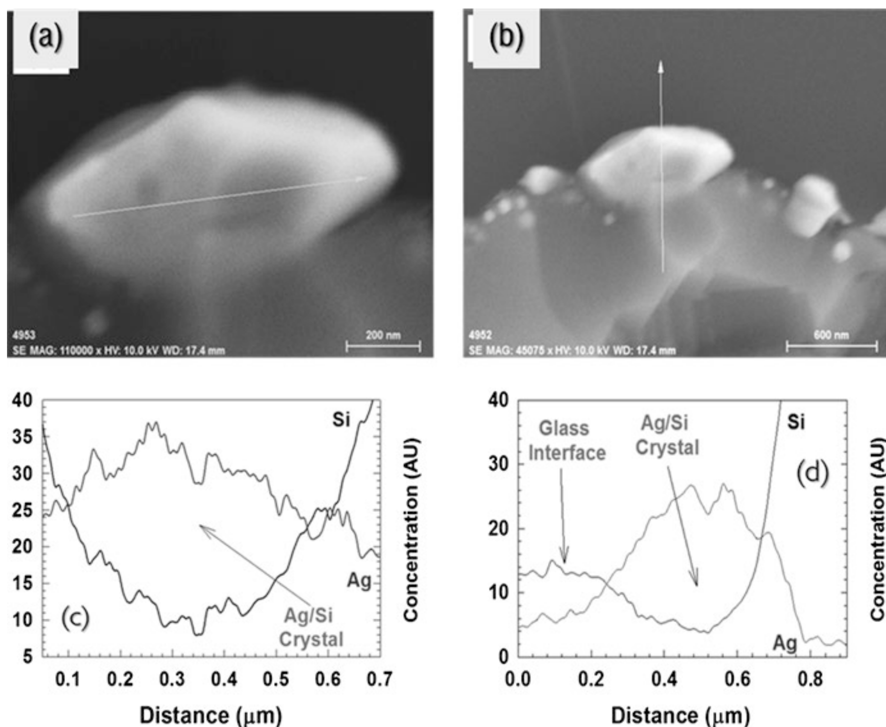

Fig. 4.66 SEM images of elliptical Ag/Si crystallite identifying direction of the EDX linescan analysis parallel (**a**, **c**) and perpendicular to the Si substrate (**b**, **d**)

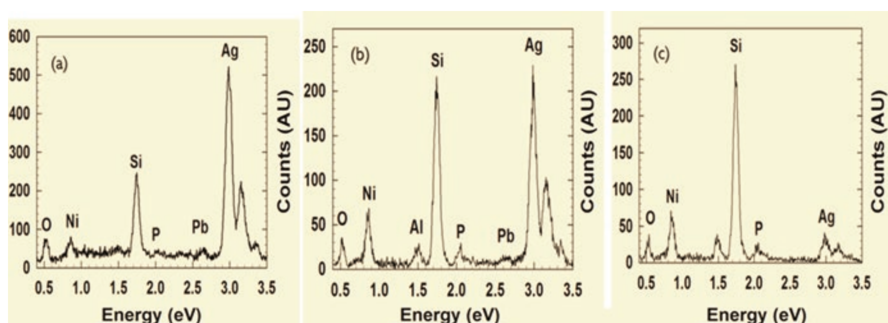

Fig. 4.67 EDX analyses of Ag-rich (**a**), comparable Ag and Si (**b**), and low Ag concentration (**c**) in Ag/Si crystallites

the glass region; large increase in Ag at the Si interface is due to the growth of Ag/Si crystal. Figure 4.69 (b and d) plots EDX linescan mapping of Ag (red line in Fig. 4.69d) and Si (black line in Fig. 4.69d) concentrations across a thin (~ 0.3 μm) glass film sandwiched between the paste and Si substrate (Fig. 4.69b). It is observed

Table 4.18 Composition variation in Ag/Si crystallites at 900 °C

Element	Concentration range (%)
O	~ 3–13
Si	~ 11–40
P	~ 0.3–4.8
Pb	~ 0.02–2
Ag	~ 2–82

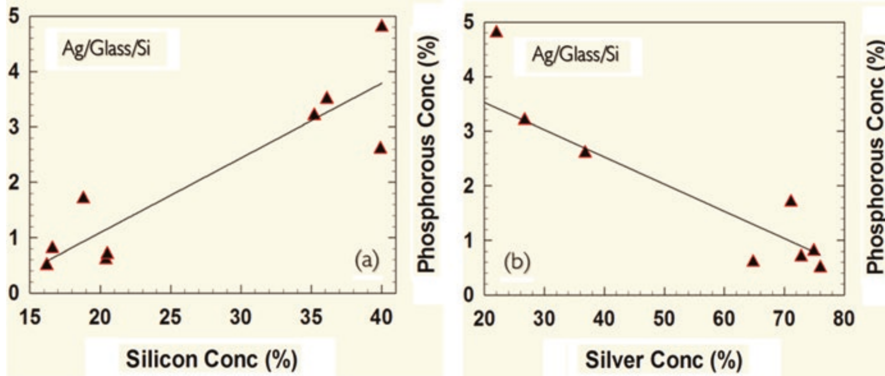

Fig. 4.68 Variation of phosphorus as a function of Si (**a**) and Ag (**b**) concentrations in Ag/Si crystallites; black line represents linear fit to the experimental data points (red triangles)

that the concentration of Ag remains invariant within the glass interface indicating presence of high density of Ag/Si crystals and reduced to insignificant values inside the glass region; large variation at paste/glass and paste/Si interfaces are attributed to presence of Ag/Si crystals. Therefore, contact resistivity increases with increased glass thickness and reduced density of Ag/Si crystalline structures.

Similar Ag/Si contact interface measurements were carried out in quartz tube configuration. Figure 4.70 plots EDX linescan mapping of Ag (red line in Fig. 4.70c) and Si (black line in Fig. 4.70c) concentrations across a thick (~ 1.5 μm) glass film sandwiched between the paste and Si substrate (Fig. 4.70a); the peak temperature was 850 °C. It is observed that the concentration of Ag is insignificant inside the glass region; concentration of Si also exhibits a steep gradient inside the glass region with concentration decreasing from its highest value of ~ 30% at Si/glass to near zero at glass/paste interface. There is also no indication of Ag/Si crystalline structures. Figure 4.70 also plots EDX linescan mapping of Ag (red line in Fig. 4.70d) and Si (black line in Fig. 4.70d) concentrations across a thin (~ 0.5 μm) glass film sandwiched between the paste and Si substrate (Fig. 4.70b); the peak temperature was 925 °C. Concentration of Ag was reduced by a factor of 6 in comparison with its value in the paste. Concentration of Si exhibits slight gradient inside the glass region with concentration decreasing from its highest value of ~ 15% at Si/glass to

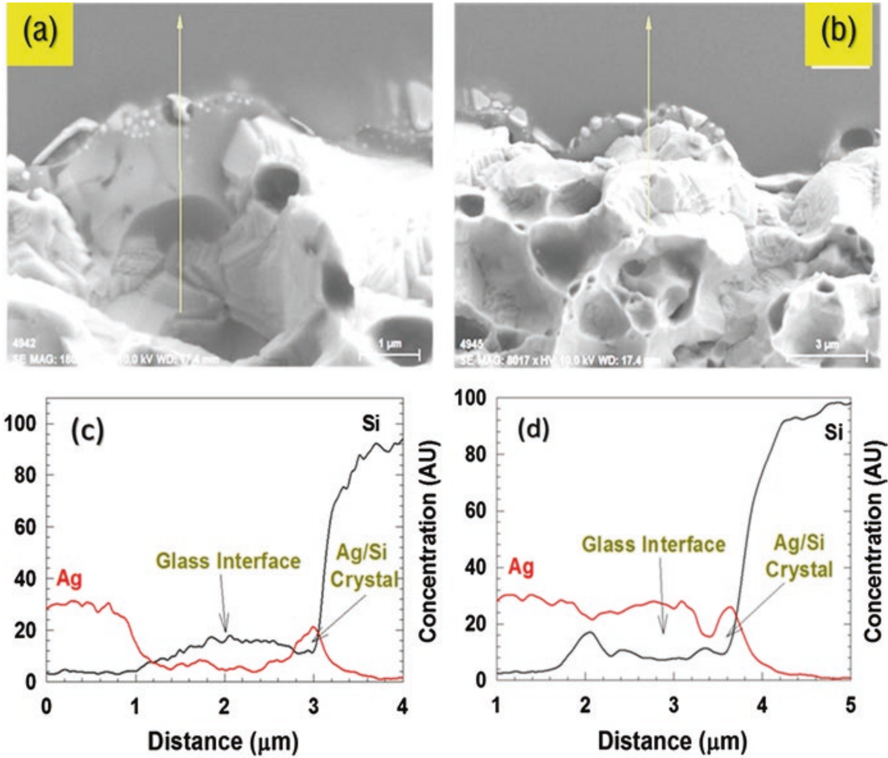

Fig. 4.69 SEM images of thick (**a**) and thin (**b**) glass films sandwiched between Ag paste and Si substrate and their respective Si and Ag concentration variation across the interface identified by yellow lines in (**c**) and (**d**); annealing was carried out in RTA configuration at 900 °C

about 10% at glass/paste interface. There is also evidence of randomly distributed nanometer-scale Ag/Si crystalline structures at the Si interface.

Large contact resistivity variation in horizontal configuration from 850 °C to 925 °C is attributed to synthesis of Ag/Si crystallites within the glass and at Si interface. The increase in contact resistivity at higher temperatures is attributed to a combination of three factors:

(i) Migration of heavily doped n-Si in the emitter region to Ag paste and Ag/Si crystallites.
(ii) Migration of Si to glass and surfaces of Ag paste.
(iii) Formation of thicker glass films with reduced density of Ag/Si crystallites.

Thermal oxidation of Si is a well-known function of temperature [52]. At temperatures below 700 °C, oxidation rate is insignificant; however, at temperatures over 850 °C and higher, it is as high as 10–20 nm/min. This rate would be higher for thin Si films with large surface areas. Therefore, a slow rise in contact resistivity at higher temperatures is attributed to oxidation of Si surfaces in paste and Ag/Si

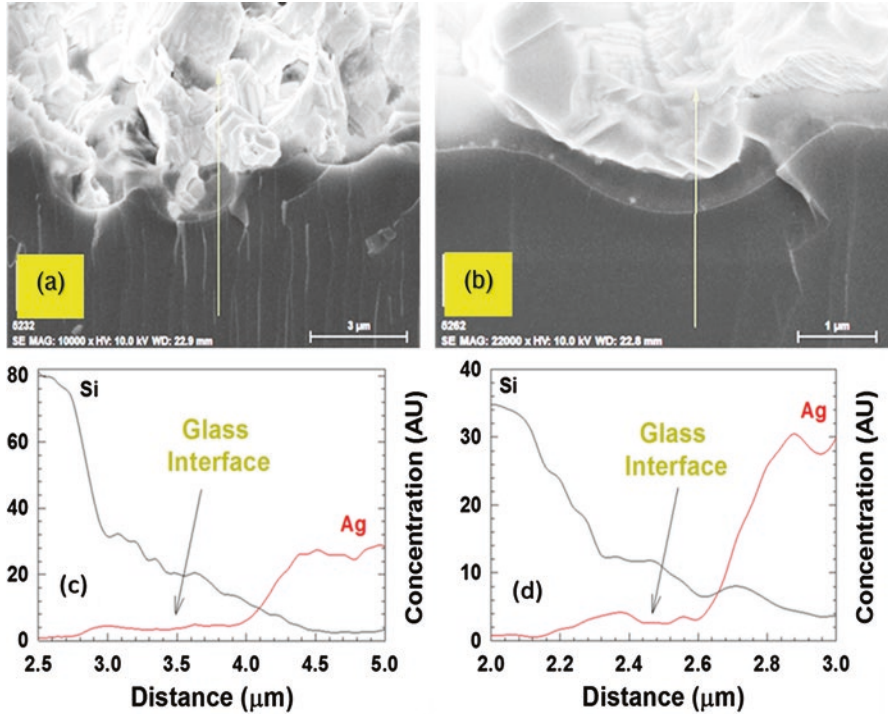

Fig. 4.70 SEM images of thick (**a**) and thin (**b**) glass films sandwiched between the silver paste and silicon substrate and their respective Si/Ag concentrations in vertical configuration at 850 °C (**a**, **c**) and 950 °C (**b**, **d**)

crystallites. Although silver is oxidized as well, it does so through a self-limiting process and is at substantially lower temperature; therefore, it is not expected to play a key role in increased contact resistivity [53].

4.10 Al/Si Contact Resistance in Vertical Configuration

In order to validate Al/Si contact interface model developed in Sect. 4.8, resistance measurements were also carried out in vertical configuration (Fig. 4.6). Figure 4.71 plots current-voltage measurements of screen-printed Al paste on both front and rear surfaces of 200-μm-thick p-type Si wafer. For these measurements, contacts were annealed in quartz tube furnace (Fig. 4.14) at 750 °C at hold times in 10–60-s range. Current-voltage response was observed to be linear with reduction in total resistance with increasing time. Measured total resistance, R_T, variation from Fig. 4.71a plotted as a function of time in Fig. 4.71b reveals logarithmic response with 93% accuracy. By neglecting R_{Si} in Eq. 4.4.19, contact resistance, R_C, is simply given by

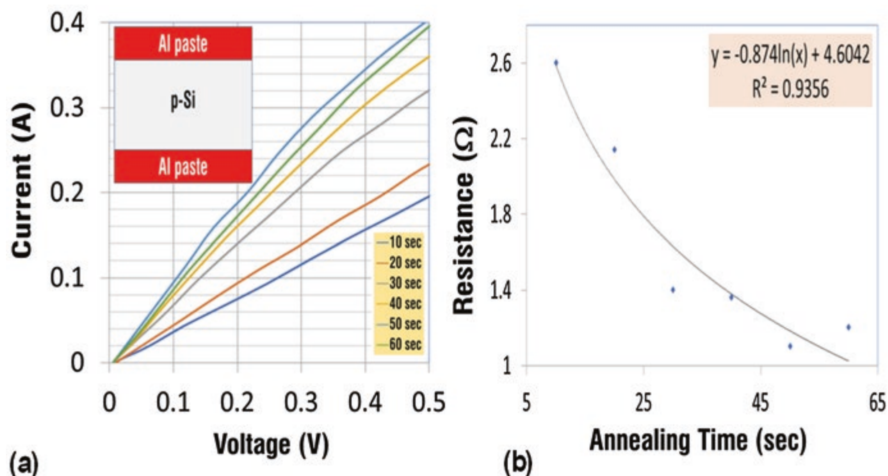

Fig. 4.71 Current-voltage measurements as a function of time for vertical Al/p-Si contact at 750 °C (**a**) and resistance variation with time (**b**)

$R_T/2$ and is ~ 0.6 Ω. Measured R_C value in vertical configuration is in good agreement with R_C values measured in TLM configurations (Figs. 4.17, 4.27, and 4.28 and Table 4.5). Therefore, in accordance with the proposed Al/Si contact model described above, increasing annealing time at fixed temperature leads to thicker Al-doped layers, hence the approximately linear reduction in resistance.

4.11 Al/Si Interface After Al Removal

Vertical resistance measurements of Al/Si contacts in Fig. 4.71 include both the Al paste and the Al/Si eutectic region (Fig. 4.51). By etching Al film, influence of the Al-doped epitaxial layer and Al-doped Si substrate can be examined. Figure 4.72 displays SEM images of Al/Si interface after removal of excess Al in HCl solution. Figure 4.72a shows boundary between Si and A/Si regions. The reduced depth (~ 10 μm) in Si/Al region is attributed to Al/Si intermixing described in Sect. 4.8.6. Figure 4.72b and 4.72c reveal varying surface features formed during Al/Si epitaxial growth process. Figure 4.72d displays cross-sectional image of Al-doped Si epitaxial film growing from the Si substrate; the thickness of this layer is estimated at ~ 3 μm. Figure 4.73 describes EDX linescan analysis of the Al/Si interface. Al and O concentrations increase close to the surface similar to that observed in Fig. 4.48. Overall, the Al/Si interface features, after removal of Al, observed in Figs. 4.72 and 4.73 are in good agreement with the Al/Si model described in Sect. 4.8. Resistance measurements of Al/Si interfaces after Al removal were carried out by screen printing polymer-based Ag paste [54]. This Ag paste is highly conductive and is annealed at 150 °C for 10 min. Figure 4.74 plots resistance variation as a function of time at

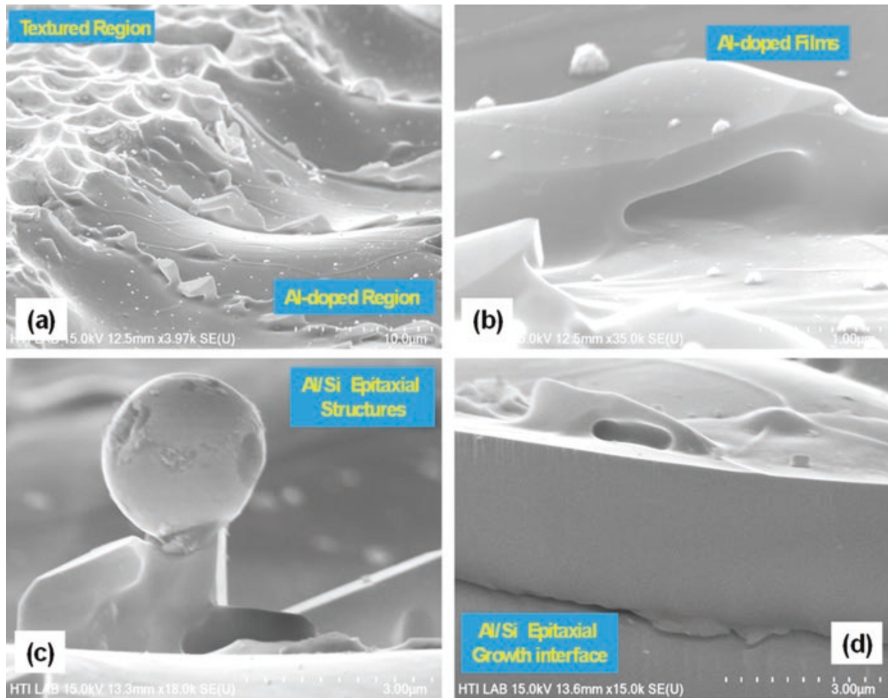

Fig. 4.72 SEM profiles of Al/Si contact interface after removal of Al illustrating formation of epitaxial growth through high temperature intermixing of Al and Si: (**a**) boundary between Al and non-Al regions, (**b**) epitaxially grown thin-film bridge, (**c**) post and spherical Al-doped film (**c**), and (**d**) cross-sectional image of epitaxial film growing from the Si substrate

fixed 750 °C temperature; R_T and R_C values have been listed in Table 4.19. Resistance response is logarithmically similar to that of Al paste (Fig. 4.71b). Both R_C and R_T resistances are higher presumably due to Ag-polymer/Al-doped surface contact resistance. Approximate linear reduction in resistance is attributed to thicker Al-epitaxial and Al-doped layers as increased annealing time.

4.12 Ag/Si Contact Resistance in Vertical Configuration

In order to further validate Ag/Si screen-printed model developed in Section 4.9, resistance measurements were carried out in vertical configuration (Fig. 4.6). Figure 4.75 plots current-voltage measurements on screen-printed Ag paste on both front and rear surfaces of 200-μm-thick n^+/n-Si wafer; sheet resistance of n^+ layer was ~ 100 Ω/square. For these measurements, contacts were annealed in quartz tube furnace (Fig. 4.14) for 10 s at peak temperatures in 750–900 °C range (Fig. 4.15). Current-voltage response was observed to be linear with reduction in total

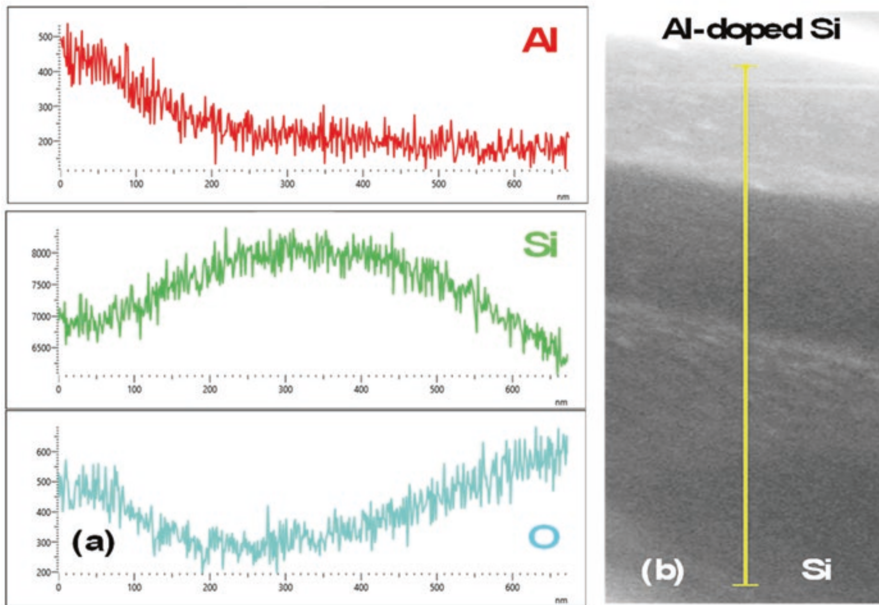

Fig. 4.73 EDX analysis of Al/Si contact interface from the top to bottom (**a**) and the image of linescan area (**b**)

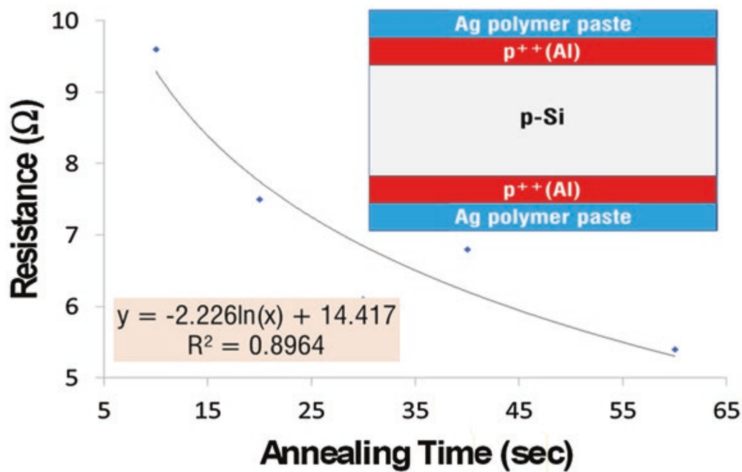

Fig. 4.74 Plot of resistance variation with time at 750 °C anneal temperature

Table 4.19 Contact resistance variations in vertical configuration at 750 °C anneal temperature

Time (sec)	R_T (Ω)	R_C (Ω)
10	9.6	4.8
20	7.5	3.75
40	6.8	3.4
60	5.4	2.7

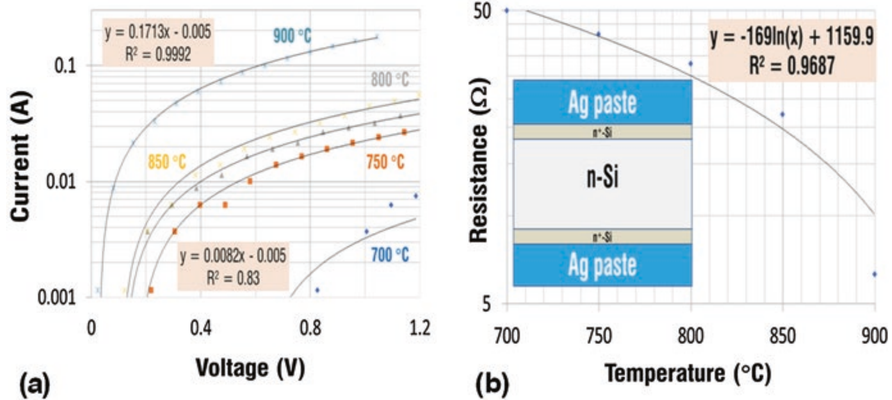

Fig. 4.75 Current-voltage measurements of Ag/Si contact as a function of temperature for fixed annealing time of 10 s (**a**) and resistance variation with temperature (**b**)

resistance with time; the current scale is plotted on logarithmic scale. At peak temperatures in 700–850 °C, barrier height decreases from ~ 0.7 V to 0.1 V as resistance decreases monotonically. Measured total resistance, R_T, variation from Fig. 4.75a plotted as a function of temperature in Fig. 4.75b reveals logarithmic response with 97% accuracy. By neglecting R_{Si} in Eq. 4.19, contact resistance, R_C, is simply given by $R_T/2$ and is ~ 3 Ω. Measured R_C value in vertical configuration is in good agreement with R_C values measured in TLM configuration (Fig. 4.34 and Table 4.5). Contact Ag/Si contact resistivity is a function of doping and increases with lower doping levels. At fixed doping level, resistance is expected to decrease at higher temperatures due to the formation of Ag/Si micro- and nanocrystallites. Therefore, reduction in R_T as a function of temperature is in good agreement with Ag/Si contact model developed in Sect. 4.9.

4.13 Ag/Si Interface After Ag Removal

Vertical resistance measurements of Ag/Si contacts in Fig. 4.75 include Ag paste, Ag-silicide, and Ag/Si crystallites (Fig. 4.58). By etching Ag film, influence of the Ag-silicide and Ag/Si crystallites can be investigated. Figure 4.76 displays SEM

images of Ag/Si contacts after removal of Ag. Figure 4.76a displays cross-sectional image of Ag-silicide at Si interface; the thickness of the film is ~ 20 nm. Ag-silicide is formed uniformly across the surface and its thickness increases only slightly with annealing temperature. Figures 4.76b and c display cross-sectional images of Ag/Si crystallites with ~ 40-nm diameter (Fig. 4.76b) at low temperatures (b) and ~ 700-nm-long and 400-nm diameter Ag/Si crystallite at higher temperatures (Fig. 4.76c). Figure 4.76d displays varying shapes in Si after removal of Ag/Si crystallites. Figure 4.77a displays SEM image of a multitude of Ag-rich Ag/Si nanostructured crystallites (diameter ~ 30 nm); EDX concentration analysis of one of the spheres is plotted in Fig. 4.77b. The concentration profiles of Ag, O, and Si are similar to those observed before Ag removal (Figs. 4.66 and 4.67); higher O concentrations after removal of Ag may be attributed to formation of native oxide films. Figure 4.78 displays SEM image of Si surface with and without Ag/Si crystallites; spectrum 4 and spectrum 6 were identified for EDX analysis in Fig. 4.79. EDX elemental concentration of region spectrum 4 (Fig. 4.79a) reveals Ag-poor region similar to that observed in Fig. 4.61. EDX map of spectrum 6 region reveals no Ag and negligible O concentration since Ag/Si crystallite has been removed. Overall,

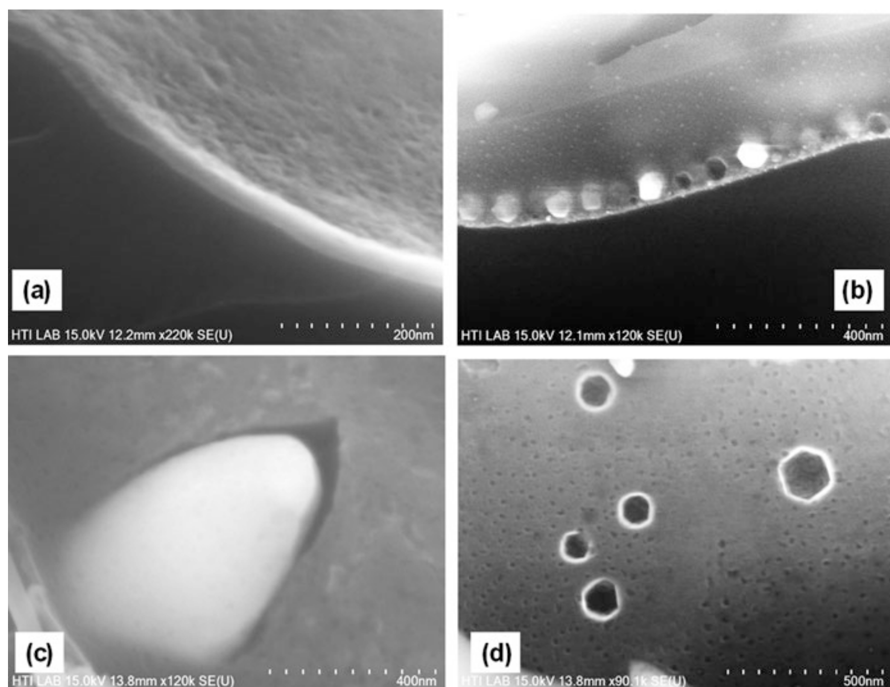

Fig. 4.76 SEM profiles of Ag/Si contact interface after removal of Ag illustrating formation: (**a**) thin Ag-silicide at Si/Ag interface, (**b**) formation of ~ 40-nm diameter Ag/Si crystallites at low temperatures (**b**), formation of ~ 700-nm-long and 400-nm diameter Ag/Si crystallite at higher temperatures, and (**d**) varying shapes in Si after Ag/Si crystallite removal

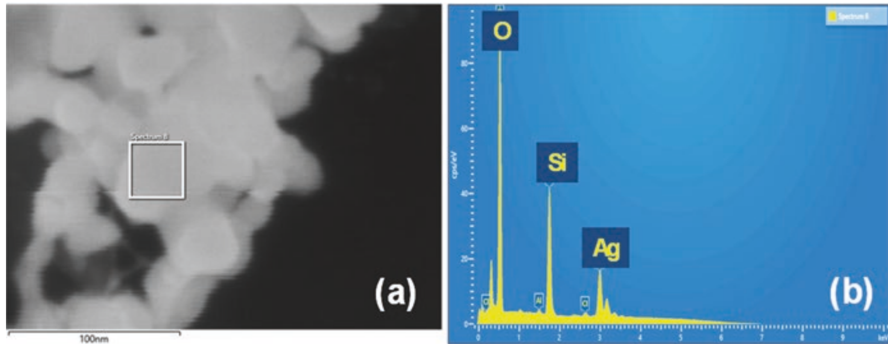

Fig. 4.77 SEM image of (**a**) Ag-rich Ag/Si nanostructured crystallites (diameter ~ 30 nm) and (**b**) its EDX analysis

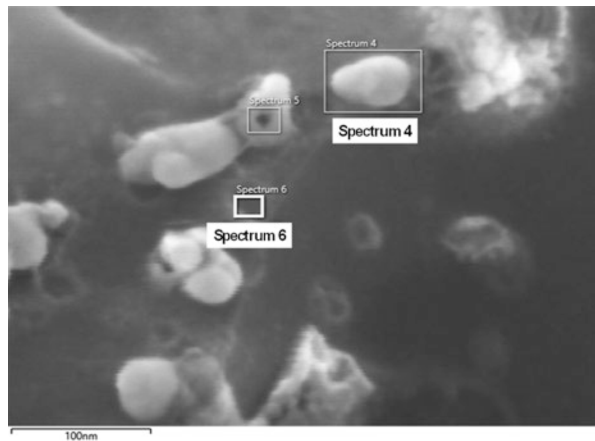

Fig. 4.78 SEM cross-sectional image of varying dimension Ag/Si micro crystallites identified for EDX analysis; crystallite diameters range from ~ 10 to 50 nm

the Ag/Si interface features are in good agreement with the Ag/Si model described in Sect. 4.9.

Vertical resistance measurements of Ag/Si interfaces after Ag removal were carried out by screen printing polymer-based Ag paste in two configurations described in Fig. 4.80. In the Ni/Si configuration (Fig. 4.80a, electroless Ni-silicide contact was formed on n^+-doped surfaces at 400 °C annealing for 5 min [55]. For shallow doping with sheet resistances ~ 100 Ω/square, high temperature annealing is not an effective option and is often replaced by low temperature silicide formation processes. In order to compare the performance of Ni-silicide contact with Ag/Si crystallites, Ni electroless contact was also formed on Ag/Si contacts after removal of Ag (Fig. 4.80b). Figure 4.81 plots current-voltage measurements for vertical contact configurations described in Fig. 4.80; for comparison, resistance measurements from screen-printed samples in Fig. 4.75 have also been included. Total resistance, R_T, and R_C have been summarized in Table 4.20; lowest contact resistance is observed for the Ni/Ag-silicide/Ag/Si crystallite configuration. Resistance

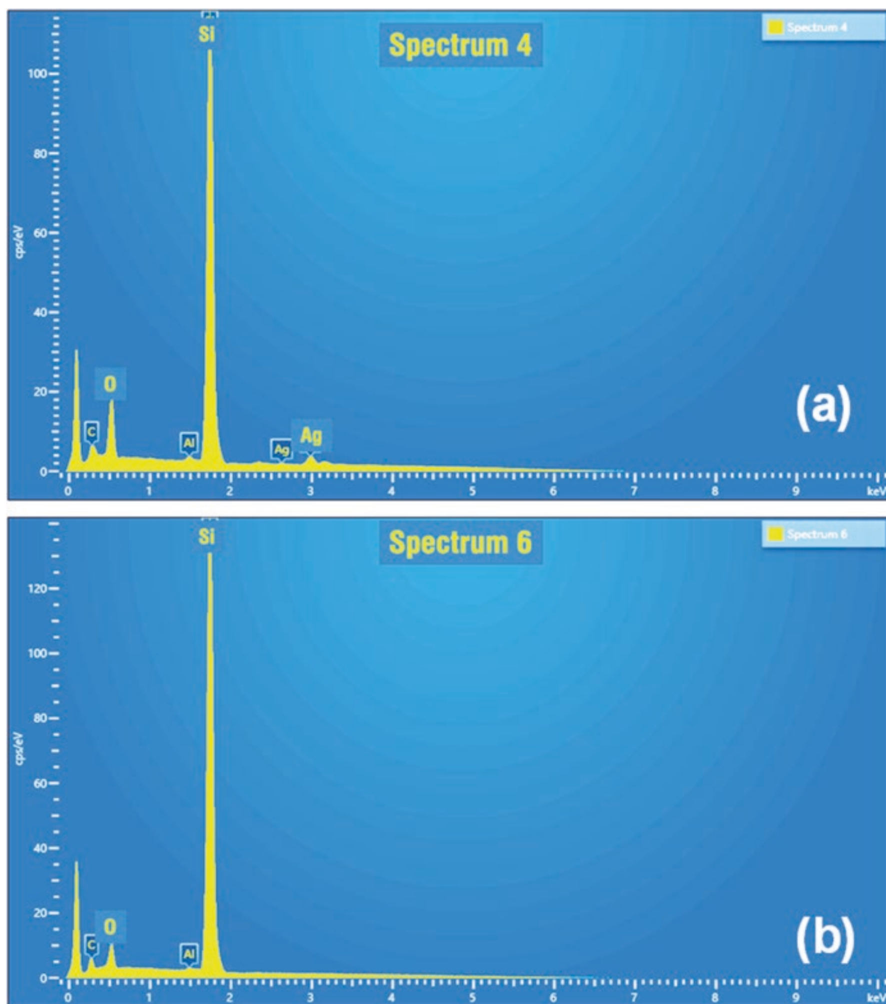

Fig. 4.79 EDX analysis of SEM image of (**a**) spectrum 4 and (**b**) spectrum 6 identified in the SEM image of Fig. 4.78

measurements reveal that for shallow-doped surfaces, Ni-silicide contact resistance is approximately 20 times lower than screen-printed Ag contact at 750 °C. Likewise, Ni-silicide contact with Ag/Si crystallites; contact resistance is approximately 25 times lower than screen-printed Ag contact at 750 °C. Lower contact resistance in configuration described in Fig. 4.80b is attributed to enhanced conductivity of Ag/Si crystallites. Therefore, SEM, EDX, and resistance measurements in this section once again reaffirm the Ag/Si contact model developed in Sect. 4.9.

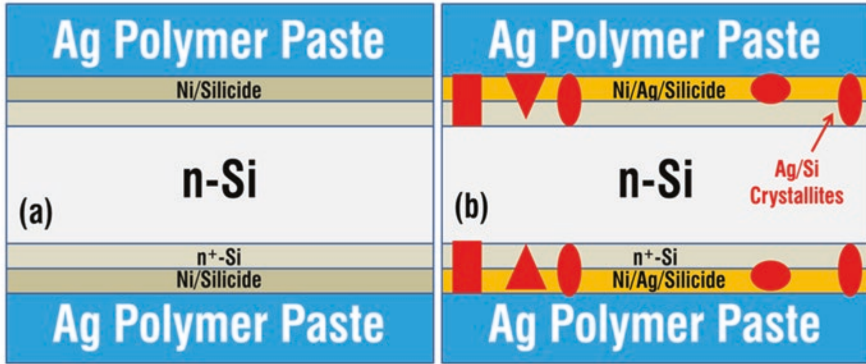

Fig. 4.80 Vertical resistance measurement configurations with (**a**) Ni/Si and (**b**) Ni/Ag-silicide/Ag/Si crystallites

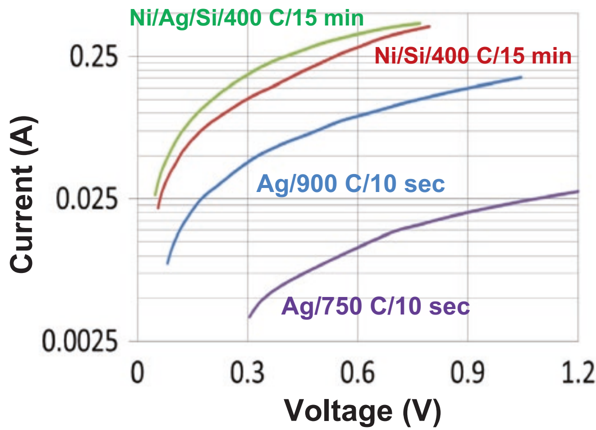

Fig. 4.81 Current-voltage measurements in three different vertical configurations: high temperature Ag/n-Si, low temperature Ni/Si, and low temperature Ni/silicide on Ag/Si crystallites after removal of Ag

Table 4.20 Contact resistances in vertical configuration on n^+/n-Si surfaces

Configuration	R_T (Ω)	R_C (Ω)
Ag/750 °C/10 s	42	21
Ag/900 °C/10 s	6.6	3.3
Ni/400 °C/15 min	2.2	1.1
Ni/Ag-silicide/Ag/Si crystallites/750 °C/10 s	1.6	0.8

4.14 Final Considerations

An in-depth investigation of electrical, morphological, and compositional characteristics of screen-printed aluminum and silver paste contacts over a broad temperature range in four geometrically and physically different thermal processing systems has been carried out. Al/Si contact formation is relatively straightforward and is based on Al/Si eutectic alloy, Al-doped Si epitaxial film, and lightly doped Al substrate. Steady-state, slow thermal variation favors formation of high-quality contact. A broad flexibility is observed in terms of both temperature and annealing time. Longer annealing time at low temperature favors superior Al/Si contact formation.

In contrast, the silver contact is based on migration of silicon into glass and paste regions, inter-mixing of Ag and Si in liquid state due to their substantially lower melting points at nanoscale dimensions. In the cooling down process, excess Si rejected into glass and paste regions is recrystallized into Ag/Si nano- and microstructures and into Ag paste. Increase in contact resistivity at higher temperatures is attributed to a combination of several factors including loss of heavily doped Si regions in the emitter region to the paste and glass regions. Density, shape, and dimensions of Ag/Si crystallites are functions of temperature with lower temperatures favor nm-scale spheres. Rapid ramp rate favors superior contact formation. It may be possible to reduce the higher contact resistance in quasi-steady-state conditions through post-metallization forming anneal in forming gas since it has been shown to facilitate Ag/Si crystals within the glass as well as on the Si interface [56].

References

1. S.N.F.A. Hamid, N.A.M. Sinin, Z.F.M. Ahir, S. Sepeai, K. Sopian, S.H. Zaidi, Mat. Res. Exp. **7**(1) (2020)
2. J. Kanga, J.S. You, C.S. Kang, J.J. Pak, D. Kim, Sol. Energy Mater. Sol. Cells **74**(91) (2002)
3. J.-H. Guo, J.E. Cotter, Sol. Energy Mater. Sol. Cells **86**(485) (2005)
4. D.-H. Neuhaus, A. Munzer, Adv OptoElect **2007**, 1 (2007)
5. W.R. Thurber, R.L. Mattis, Y.M. Liu, J.J. Filliben, J. Electrochem. Soc. **127**, 1807 (1980)
6. D.K. Schroder, *Semiconductor Material and Device Characterization*, 2nd edn. (Wiley, 1998)
7. E.H. Rhoderick, *Metal-Semiconductor Contacts* (Oxford University Press, 1978)
8. C.Y. Chung, Y.K. Fang, S.M. Sze, Solid State Electron. **14**, 541 (1971)
9. A. Scorzonie, M. Finetti, Mat. Sci. Rep. **3**, 79 (1988)
10. W.J. Boudville, T.C. McGill, J. Vac. Sci. Technol. B **3**, 1192 (1985)
11. S.M. Ahmad, C. Siu, Leong, R.W. Winder, K. Sopian, S.H. Zaidi, J. Electron. Mater. **47**, 6791 (2018)
12. S.M. Ahmad, C. Siu, Leong, R.W. Winder, K. Sopian, S.H. Zaidi, J. Electron. Mater. **48**, 6382 (2019)
13. https://en.wikipedia.org/wiki/Gompertz_function
14. B. Sopori, V. Mehta, P. Rupnowski, H. Moutinho, A. Shaikh, C. Khadilkar, M. Bennett, D. Carlson, MRS Proceedings **1123**, 5 (2008)
15. I. Egry, Scr. Metall. Mater. **28**, 1273 (1993)
16. J.L. Murray, A.J. McAlister, Bull. Alloy Phase Diagr. **5**, 74 (1984)
17. T. Yoshikawa, K. Morita, J. Electrochem. Soc. **150**, 465 (2003)

18. O. Krause, H. Ryssel, P. Pichler, J. Appl. Phys. **91**, 5645 (2002)
19. F. Huster, 20th EUPVSEC (2005).
20. V.A. Popovich, M.P.F.H.L. van Maris, M. Janssen, I.J. Bennett, I.M. Richardson, Mater. Sci. Appl **4**, 118 (2013)
21. M. Balucani, L. Serenelli, K. Kholostov, P. Nenzi, M. Miliciani, F. Mura, M. Izzi, M. Tucci, Energy Procedia **43**, 100 (2013)
22. E. Urrejola, K. Peter, H. Plagwitz, G. Schubert, Appl. Phys. Lett. **98**, 96 (2011)
23. J. Krause, R. Woehl, M. Rauer, C. Schmiga, J. Wilde, D. Biro, Sol. Energy Mater. And Solar Cells **95**, 2151 (2011)
24. T. Lauermann, B. Frohlich, G. Hahn, B. Terheiden, Prog. Photovolt **23**, 10 (2015)
25. G.K. Reeves, H.B. Harrison, IEEE Electron Device Lett. **3**, 111 (1982)
26. S. Wu, W. Wang, L. Li, D. Yu, L. Huang, W. Liu, RSC Adv. **24384** (2014)
27. M. Prudenziati, L. Moro, B. Morten, F. Sirotti, L. Sardi, Act. Passiv. Electron. Components **13**, 133 (1989)
28. B. Thuillier, J.P. Boyeaux, A. Kaminski, A. Laugier, Mater. Sci. Eng. B Solid-State Mater. Adv. Technol **102**, 58 (2003)
29. C. Ballif, D.M. Huljić, G. Willeke, A. Hessler-Wyser, Appl. Phys. Lett **82**, 1878 (2003)
30. M.M. Hilali, K. Nakayashiki, C. Khadilkar, R.C. Reedy, A. Rohatgi, A. Shaikh, S. Kim, S. Sridharan, J. Electrochem. Soc **153**, A5 (2006)
31. C.H. Lin, S.Y. Tsai, S.P. Hsu, M.H. Hsieh, Sol. Energy Mater. & Sol. Cells **92**, 1011 (2008)
32. Z.G. Li, L. Liang, L.K. Cheng, J. Appl. Phys **105**, 19 (2009)
33. K. Hong, S. Cho, J.S. You, J. Jeong, S. Bea, J. Huh, Sol. Energy Mater. Sol. & Cells **93**, 898 (2009)
34. S. Kontermann, M. Hörteis, M. Kasemann, A. Grohe, R. Preu, E. Pink, T. Trupke, Sol. Energy Mater. Sol. & Cells **93**, 1630 (2009)
35. M.I. Jeong, S.-E. Park, D.-H. Kim, J.-S. Lee, Y.-C. Park, K.-S. Ahn, C.-J. Choi, J. Electrochem. Soc. **157**, H934 (2010)
36. E. Cabrera, S. Olibet, J. Glatz-Reichenbach, R. Kopecek, D. Reinke, G. Schubert, J. Appl. Phys. **110**, 114511 (2011)
37. M. Eberstein, H. Falk-Windisch, M. Peschel, J. Schilm, T. Seuthe, M. Wenzel, C. Kretzschmar, U. Partsch, Energy Procedia **27**, 522 (2012)
38. W. Wu, C. Chan, M. Lewittes, L. Zhang, and K. Roelofs, Energy Procedia, vol. 92, 984 (2016).
39. J.D. Fields, M.I. Ahmad, V.L. Pool, J. Yu, D.G. Van Campen, P.A. Parilla, M.F. Toney, M.F.A.M. van Hest, Nat. Commun. **7**, 11143 (2016)
40. P. Kumar, M. Pfeffer, B. Willsch, O. Eibl, L. Yedra, S. Eswara, J.N. Audinot, T. Wirtz, Sol. Energy Mater. & Sol. Cells **160**, 398 (2017)
41. D. K. Sarkar, S. Dhara, K. G. M. Nair, and S. Chowdhury, Nucl. Instruments Methods Phys. Res. Sect. B Beam Interact. with Mater. Atoms 168, 215 (2000).
42. G. Utlu, N. Artunç, Appl. Surf. Sci. **310**, 248 (2014)
43. F. Rollert, N.A. Stolwijk, H. Mehrer, J. Phys. D. Appl. Phys. **20**, 1148 (1987)
44. L. Chen, Y. Zeng, P. Nyugen, T.L. Alford, Mater. Chem. Phys. **76**, 224 (2002)
45. L. Weber, Metall. Mater. Trans. A **33**, 1145 (2002)
46. S. W. Jones, Silicon circuit process technology 38, No. 9, IC Knowledge LLC, 3475 (2008).
47. M. Van Craen, L. Frisson, F.C. Adams, Surf. Interface Anal. **6**, 257 (1984)
48. A. Hiraki, E. Lugujjo, J. Vac. Sci. Technol. **9**, 155 (1971)
49. J.W. Tringe, G. Vanamu, S.H. Zaidi, J. Appl. Phys. **104** (2008)
50. M. Asoro, J. Damiano, P. Ferreira, Microsc. Microanal. **15**, 706 (2009)
51. M.S. Martin, N.D. Theodore, C.-C. Wei, L. Shao, Sci. Rep. **4**, 6744 (2014)
52. R.C. Jaeger, *Introduction to Microelectronic Fabrication* (Prentice-Hall, Inc., 2002)
53. M.L. Zheludkevich, G. Gusakov, G. Voropaev, A. Vecher, E.N. Kozyrski, S. Raspopov, Oxid. Met. **61**, 39 (2004)

54. https://www.ferro.com/products/product-category/electronic-materials/polymer-thick-film-pastes-and-specialties/conductive-paints_lacquers-and-pastes/silver-conductive-pastes
55. D.S. Kim, E.J. Lee, J. Kim, S.H. Lee, Journal of the Korean Physical Society **46**, 1208 (2005)
56. S. Bin Cho, H.S. Kim, J.Y. Huh, Acta Mater **70**, 1 (2014)